Acta Pharmaceutica Sinica B 2026;16(2):1090−1115

Chinese Pharmaceutical Association
Institute of Materia Medica, Chinese Academy of Medical Sciences

Acta Pharmaceutica Sinica B

www.elsevier.com/locate/apsb
www.sciencedirect.com

ORIGINAL ARTICLE

Intratumoral immune-microbial crosstalk shaped by tumor cell-derived extracellular vesicles encapsulating berberine boosts lung cancer immunotherapy

Jingjing Deng[a,b,c,d,†], Wenlong Kuang[e,f,†], Wenjuan Chen[a,b,c,d,†], E. Zhou[a,b,c,d,†], Yali Wu[a,b,c,d,†], Zimo Yang[a,b,c,d], Jiangbin Chen[a,b,c,d], Xinghui Cao[a,b,c,d], Zhengrong Yin[a,b,c,d], Jiatong Liu[a,b,c,d], Minglei Li[a,b,c,d], Feng Wu[a,b,c,d], Jinshuo Fan[a,b,c,d], Mengfei Guo[a,b,c,d,*], Yang Jin[a,b,c,d,*]

[a]*Department of Respiratory and Critical Care Medicine, Hubei Province Clinical Research Center for Major Respiratory Diseases, NHC Key Laboratory of Pulmonary Diseases, Union Hospital, Tongji Medical College and State Key Laboratory for Diagnosis and Treatment of Severe Zoonostic Infectious Disease, Huazhong University of Science and Technology, Wuhan 430000, China*
[b]*MOE Key Laboratory of Biological Targeted Therapy, Union Hospital, Tongji Medical College, Huazhong University of Science and Technology, Wuhan 430000, China*
[c]*Hubei Province Engineering Research Center for Tumor-Targeted Biochemotherapy, Union Hospital, Tongji Medical College, Huazhong University of Science and Technology, Wuhan 430000, China*
[d]*Hubei Key Laboratory of Biological Targeted Therapy, Union Hospital, Tongji Medical College, Huazhong University of Science and Technology, Wuhan 430000, China*
[e]*Department of Cardiology, Traditional Chinese and Western Medicine Hospital of Wuhan, Tongji Medical College, Huazhong University of Science and Technology, Wuhan 430022, China*
[f]*Department of Cardiology, Wuhan No. 1 Hospital, Wuhan 430022, China*

Received 17 March 2025; received in revised form 8 July 2025; accepted 19 July 2025

*Corresponding authors.
E-mail addresses: guomengfei19881204@163.com (Mengfei Guo), whuhjy@126.com (Yang Jin).
[†]These authors made equal contributions to this work.
Peer review under the responsibility of Chinese Pharmaceutical Association and Institute of Materia Medica, Chinese Academy of Medical Sciences.

https://doi.org/10.1016/j.apsb.2025.12.014

KEY WORDS

Intratumoral microbiome;
Personalized medicine;
Antibiotics;
Tumor microenvironment;
Tumor cell-derived extracellular vesicles;
Berberine;
Lung cancer;
Immunotherapy

Abstract The intratumoral microbiome plays a crucial role in cancer progression, prompting the development of therapies targeting it. However, due to the heterogeneous effects of intratumoral microbes, designing treatments tailored to the unique microecological characteristics of individual tumors poses a significant challenge. Here, we found significant variations in the abundance of five bacterial genera—*Lysinibacillus*, *Stenotrophomonas*, *Weissella*, *Comamonas*, and *Aeromonas*—between lung adenocarcinoma (LUAD) and normal tissues by analyzing single-cell transcriptomic datasets. These specific bacterial clusters were significantly associated with immune infiltrates in the tumor microenvironment (TME). After confirming their effects in mouse models, these bacterial taxa were identified as potential therapeutic targets. Through *in vitro* drug screening assays, berberine was identified as a promising agent that selectively inhibits harmful bacteria while sparing beneficial ones. To address berberine's low solubility and tumor targeting issues, it was encapsulated into tumor cell-derived extracellular vesicles (EV-ber). Feature analysis demonstrated that EV-ber shifted the intratumoral microbiome profile toward an anti-tumor phenotype and enhanced anti-tumor immunity in the TME. Furthermore, EV-ber administration inhibited LUAD growth, impaired LUAD metastatic ability, and boosted the effectiveness of anti-PD-L1 immunotherapy in mouse models. In conclusion, this work demonstrates the potential of personalized intratumoral microbial re-education strategies in LUAD therapy.

1. Introduction

Despite notable advancements in therapeutic practices over the past decade, lung cancer remains a formidable challenge, requiring the ongoing pursuit of more effective therapies[1,2]. Recently, with the development of detection technology and an in-depth understanding of TMEs, the presence of intratumoral microbiomes has been confirmed by accumulating evidence[3,4]. Studies have shown that intratumoral bacteria may promote tumorigenesis and progression in several ways, including direct effects on transcriptional pathways of inflammation, tumor growth, and immune cell infiltration. For instance, Fu et al.[5] reported that *Staphylococcus*, *Lactobacillus*, and *Streptococcus* were enriched in breast cancer cells, enabling tumor cells to resist mechanical stress within blood vessels and thereby promoting metastasis. Moreover, the intratumoral microbiome contributes to the formation of an immunosuppressive microenvironment, which can lead to treatment resistance[6]. Consequently, targeting intratumoral bacteria has emerged as a focal point in cancer research.

Recent efforts to target the intratumoral microbiota have primarily focused on clearing tumor-infiltrating microbes, with early results showing some promising outcomes. For instance, Bullman et al.[7] demonstrated that metronidazole, a clinically approved antibiotic for treating anaerobic bacterial infections, significantly reduced *Fusobacterium* load and slowed tumor growth in *Fn*-enriched xenograft models. However, systemic antibiotic administration may disrupt the balance of the microbiota and contribute to the development of drug resistance. Furthermore, increasing clinical evidence suggests that systemic antibiotic use can diminish the efficacy of immune checkpoint inhibitors[8,9]. These seemingly contradictory findings underscore the complexity of the tumor microenvironment and highlight the heterogeneity of the intratumoral microbiome.

Interestingly, in contrast to their pro-tumor effects, certain intratumoral bacteria have been shown to exert anti-tumor benefits. A recent study revealed that intratumoral *Bifidobacterium* can activate dendritic cells (DCs) *via* the STING signaling pathway, offering novel insights into how intratumoral bacteria may enhance the efficacy of T cell-directed immunotherapy[10]. Additionally, the presence of *Saccharopolyspora*, *Pseudoxanthomonas*, and *Streptomyces* in pancreatic adenocarcinoma tissues has been associated with enhanced anti-tumor immune responses through the recruitment and activation of $CD8^+$ T cells[11]. Clinically, microorganism-associated cancers, particularly HPV-positive head and neck squamous cell carcinoma (HNSCC), have been linked to improved survival rates, increased frequencies of tertiary lymphoid structures, and enhanced B cell activity compared to HPV-negative HNSCC[12]. Therefore, considering the dual roles of the intratumoral microbiome, developing strategies to classify intratumoral microbiomes into harmful and beneficial subtypes could significantly improve targeted therapeutic approaches.

Bacterial characteristics identified in large-scale population studies often fail to be consistently replicated in individual patients. Given the heterogeneity among patients, it is essential to identify target bacteria within individual tumors to develop effective intervention strategies. A comprehensive investigation of microbiota−host interactions at the single-cell level between tumor and normal lung tissues can aid in the classification of intratumoral bacteria. By analyzing single-cell transcriptomic datasets from lung cancer patients, microbial and immune signatures at the cellular level can be characterized. Understanding the crosstalk between the immune system and microbial communities is crucial for subtyping and plays a pivotal role in designing therapies tailored to the unique microecological features of individual tumors.

In this study, we first delineated the profiles of intratumoral microbiomes by analyzing single-cell transcriptomic datasets from lung cancer patients. Through the analysis of intratumoral immune−microbial interactions, we identified specific bacterial candidates of interest. Guided by the principle of "selectively eliminating harmful microbes while preserving beneficial ones", we leveraged a compound library screening and identified berberine as a promising candidate for our intratumoral microbial remodeling strategy. Furthermore, berberine was successfully encapsulated into tumor cell-derived extracellular vesicles (EV-ber) to improve its solubility and tumor-targeting efficiency for *in*

vivo applications. Immune signature analysis revealed that EV-ber significantly enhanced anti-tumor immunity within the TME. Microbial profiling demonstrated that EV-ber shifted the intratumoral microbiome composition toward an anti-tumor phenotype by reducing harmful microbes and promoting beneficial ones. *In vivo* experiments showed that EV-ber administration inhibited subcutaneous tumor growth, synergized with anti-PD-L1 immunotherapy to enhance antitumor effects, and impaired tumor metastatic potential in mouse models. In conclusion, this work demonstrates the possibility and potential of customized intratumoral microbial re-education strategies in LUAD therapy.

2. Methods and materials

2.1. Bioinformatics analysis

2.1.1. Corhort selection and metagenomic classification

This study primarily analyzed data from two scRNA-seq datasets[13,14], in which 10 human LUAD and 10 normal lung tissues were analyzed, totally. There was no randomization or blinding during data analysis and sample size estimation or power computations were not applicable. The samples were checked for batch effects at the levels of sample and somatic cell type clusters. The cohort had around 25 million reads per sample, of which a substantial proportion did not map to the human genome, and these reads were used for metagenomic analyses.

2.1.2. Detection and denoising of microbial sequences from scRNA-seq data

Using the SAHMI pipeline to identify and denoise microbial signals from single-cell transcriptomic sequencing of host tissues. Built upon Kraken2Uniq[15] and multiple statistical tests, SAHMI utilizes a comprehensive approach to distinguish genuine microbes residing within host cells. The pipeline leverages genome databases available from the official Kraken2 website (https://ccb.jhu.edu/software/kraken2/), and fungi genomes are sourced from our curated database. SAHMI takes raw scRNA-seq reads as input, and outputs cell barcodes associated with microbial presence.

2.1.3. Sequencing read alignments and quality control

Reads from single cells isolated using 10x chromium were demultiplexed and then aligned to the GRCh38.p12 human reference (from 10x Genomics) using Cell Ranger (version 7.1.0, 10x Genomics). Cells with fewer than 250 genes detected were excluded from further analyses. Additionally, the cells with mitochondrial percent beyond 25% were also filtered. Moreover, UMAP was created by sample integration with Harmony, an algorithm (R program) that projects cells into a shared embedding in which cells were grouped by cell types rather than dataset-specific conditions.

2.1.4. scRNA-seq data processing

All scRNA-seq data processing was done using CellRanger and Seurat[16] with default parameters, in brief, data were normalized per cell and 2000 highly variable genes were identified using the FindVariableFeatures function. Principal component analysis was performed separately using this data and uniform manifold approximation and projection plots were created using the first 30 principle components and default parameters. Cell-type annotations for data were used from the original study.

2.1.5. Differential analysis and enrichment analysis

Differential gene expression analysis was performed using the Wilcoxon rank-sum test to investigate the transcriptomic differences between cells with and without bacteria or fungi. Genes with an adjusted P value less than 0.05 and a $\log_2$ FC greater than 1 were considered as significantly differentially expressed genes. Functional enrichment analysis of differentially expressed genes was conducted using Gene Ontology (GO). Pathways with a P value less than 0.05 were considered significantly enriched.

2.2. Chemical reagents

The antibodies, chemicals, commercial kits, and other reagents used in this study are listed in detail in Supporting Information Table S1. Here, only the key reagents are described. A compound library (HY-LD-000005655) containing 281 compounds with reported antibacterial and anti-tumor activities, as well as berberine chloride hydrate (HY-17577), was purchased from MedChemExpress (MCE), Shanghai, China. The compound library was provided in a 96-well plate format, containing 10 mmol/L stock solutions of each compound in dimethyl sulfoxide (DMSO), and was stored at −80 °C.

2.3. Bacteria strains and culture

All strains were purchased commercially from Mingzhoubio, Ningbo, China. *Lysinibacillus sphaericus* (*L. sphaericus*, ATCC No. 4525), *Stenotrophomonas maltophilia* (*S. maltophilia*, CCUG No. 5866T), *Aeromonas veronii* (*A. veronii*, ATCC No. 35624), and *Comamonas testosteroni* (*C. testosteroni*, ATCC No. 55744) were all cultured in an incubator at a constant temperature of 30 °C for 24−48 h. Except for *C. testosteroni* was cultured in Brain Heart Infusion (BHI) medium, the others were all cultured in LB broth. *Weissella_cibaria* (*W. cibaria*, DSM No. 15878) and *Streptococcus_mutans* (*S. mutans*, DSM No. 20523) were cultured in MRS broth and BHI, respectively, on a constant temperature shaker at 37 °C (160 rpm) for 24−48 h and 48−72 h, respectively. Turbidimetry was used to quantify bacteria.

2.4. Antibacterial drug library screening

The library was screened at a single concentration point to identify antibacterial hit compounds against *L. sphaericus*, *S. maltophilia*, *W. cibaria* and *C. testosteroni*. Briefly, 5 μL of the standardized inoculum (corresponding to 0.5×10^5 to 1×10^5 CFU/well) were added to each well of a 96-well polystyrene microtiter plate containing 95 μL of LB, BHI or MRS with 1 μL of a 10 mmol/L compound stock solution from the MedChemExpress library, achieving a final drug concentration of 0.1 mmol/L. Uninoculated samples with 1% DMSO (final back ground in each well) were considered blank. Positive control was also prepared with 50% DMSO to yield 100% killing. The content of each well was mixed by pipetting, and plates were incubated at 37 °C under 5% CO_2. After 24 h-incubation, the survival rate of planktonic cells was assessed by optical density at 600 nm (OD600). The percentage of surviving cells was calculated compared to the inoculated, but not treated, control sample (100% survival). The antibacterial activity of library drugs was classified based on the relative viability compared to the untreated control sample[17,18]: (i) inhibiting efficacy, $\leq$25%; (ii) promoting efficacy, $\geq$100%.

2.5. Drug screening validation

The results from each HTS microplate were validated by calculating the *Z*-factor. To validate the degree of separation, the *Z*-factor and the percentage of inhibition of the positive and negative controls were determined using Eq. (1):

$$\text{Z-factor} = 1\text{-}\frac{3(\sigma p + \sigma n)}{\mu p - \mu n} \quad (1)$$

where σp and σn are the standard deviations of the positive and negative controls, respectively, and μp and μn are the corresponding mean values. A Z-factor between 0.5 and 1.0 indicates an excellent assay and statistically reliable separation between the positive and negative controls[18,19].

2.6. Bacteria viability assay

The density of the bacteria culture required for the test was adjusted to a 0.5 McFarland standard (1.0×10^8 CFU/mL) in 10 mL broth using a turbidimeter. The inoculum suspensions were dispensed in each well containing approximately 1×10^6 CFU/well. Berberine at a series of gradient concentrations was added into wells, with 0.1% DMSO serving as the control. The results were obtained by detecting the absorbance values at 600 nm after 24 h incubation.

2.7. Cell lines and cell culture

Murine Lewis lung carcinoma cell line (LLC, ATCC No. CRL-1642), human NSCLC cell lines NCI-H1975 (ATCC No. CRL-5908), A549 (ATCC No. CCL-185) and NCI-H1299 (ATCC No. CRL-5803) and human normal lung epithelial cell line HBE (ATCC No. CRL-2078) were purchased from American Type Culture Collection (ATCC). LLC-GFP cells were established by negative control lentivirus (with GFP) transfection. LLC/LLC-GFP cells and human cell lines were cultured with Dulbecco's modified Eagle's medium (DMEM; Gibco, Shanghai, China) and Roswell Park Memorial Institute (RPMI) 1640 medium (Gibco), respectively, supplemented with 10% Fetal Bovine Serum (FBS; New-zerum, NCS-500, Christchurch, New Zealand) at 37 °C in 5% CO_2-95% air.

2.8. Cell viability assay

Cell survival rates were estimated *via* CCK-8 assay. Briefly, ~3000 cells were seeded in 96-well plates containing 100 μL of the culture medium in each well overnight. After culturing with different doses of berberine for 24 h, each well was incubated with 100 μL of the medium containing 10 μL CCK-8 solution for around 1 h. Thereafter, absorbance measurements were performed at 450 nm.

2.9. Colony formation assay

Around 1000 cells were seeded in 6-well plates overnight. After incubation with different concentrations of Ber or EV-ber for 24 h, the cells were then cultured in the absence of drugs for an additional 5 days. Foci formation was determined by 0.5% crystal violet staining.

2.10. Cell apoptosis analysis

Around 50,000 cells per well were seeded in 12-well plates overnight. After incubation with different concentrations of Ber or EV-ber for 48 h, the cells were harvested *via* trypsinization without EDTA and washed twice with PBS. Thereafter, they were resuspended in 200 μL of the binding buffer and stained with 2 μL Annexin V-FITC and 2 μL propidium iodide (PI) at room temperature in the dark for 15 min. Subsequently, they were detected by flowcytometry (FACS LSRII, BD Bioscience, CA, USA) and analyzed by Flowjo (V10, BD Bioscience, CA, USA).

2.11. Preparation of EV-ctrl and EV-ber

The method for extracting EVs was documented in our previous publications[20−23]. Briefly, LLC and H1975 cells were cultured in 15-cm culture dishes for 24 h with 80% density and then exposed to ultraviolet (UVB, 300 Jm-2) irradiation in FBS-free medium for 30 min. After 24 h of incubation in FBS-free medium, supernatants were collected, and subsequently centrifuged for 10 min at 800 rpm to get rid of cells, and then centrifuged for 30 min at $2000\times g$ to remove debris. The supernatant was further centrifuged for 60 min at $16{,}000\times g$ to pellet extracellular vesicles (EVs). The pellets were washed twice and resuspended in sterile PBS.

For the loading of berberine into extracellular vesicles (EVs), 100 μg purified EVs and 200 μg Ber were gently mixed in 800 μL cold PBS. The mixture was subjected to electroporation at 350 V and 150 μF using 0.4 cm electroporation cuvettes, followed by incubation at 37 °C for 30 min to allow complete recovery of the EV plasma membrane[24]. To remove the unincorporated free berberine, the EVs were then washed with cold PBS twice prior to ultracentrifugation at $20{,}000\times g$ for 45 min. The pellets were then resuspended in sterile PBS.

2.12. Nanoparticle tracking analysis (NTA)

To evaluate the concentration and size of EVs, nanoparticle tracking analysis (PMX-120, Particle Metrix, Germany) were utilized within 24 h after EVs or EV-ber preparation. The samples were 2000 × diluted. The laser wavelength was set at 520 nm and filter wavelength as scatter to gain videos about size distribution and concentration.

2.13. Resistance pulse sensor (RPS)

The samples (at a concentration of 0.6 mg/mL) were diluted 100-fold to 6 μg/mL using NanoCoulter diluent as the buffer. 200 μL of the diluted sample was loaded for detection. Use the Nano-Coulter particle size analyzer (RESUNTECH, Shenzhen, China) for detection. Each sample was tested three times and then the average value was taken.

2.14. Transmission electron microscope (TEM)

20 μL resuspended samples were added dropwise to 200-mesh grids and incubated at room temperature for 10 min, then the grids were negatively stained with 2% phosphotungstic acid for 3 min, and the remaining liquid was removed by filter paper. Then they were observed with a transmission electron microscope (HT7700, HITACHI, Japan).

2.15. Nano-flowcytometry (nFCM)

LLC EV samples were analyzed by the nFCM (NanoFCM, Xiamen, China)[25]. Briefly, the EVs were incubated with FITC-labeled anti-mouse CD63 or EpCAM antibody (BD Pharmingen) for 2 h at room temperature in the dark and ultracentrifuged at 16,000×*g* for 90 min to remove the unbound antibodies. The pellet was then resuspended in 50 μL of PBS for phenotype analysis.

2.16. High-performance liquid chromatography (HPLC)

First, 200 mg berberine-packaged EVs were resuspended in 1 mL PBS and then analyzed using a HPLC system (LC-20AD, Shimadzu, Japan) on a C18 column (ZORBAX Eclipse XDB, Agilent, CA, USA). The mobile phase was 0.05 mol/L KH_2PO_4, 10% acetonitrile, pH 3.5, and the flow rate was 1 mL/min. The column temperature was maintained at a constant 40 °C, and Ber was detected by UV absorption at 345 nm. Detection and integration of chromatographic peaks were performed using CBM-20Alite System Controller.

2.17. BCA assay and western blotting

BCA assay was utilized to quantify the mass of EVs. The experimental procedures were followed by the instructions from the manufacture. A total of 30 μg of EVs or cell lysates was resuspended in 5 × SDS loading buffer, subsequently incubated at 95 °C for 5 min and centrifuged at 16,000×*g* for 30 min. Then, the supernatants were separated by 10% SDS-polyacrylamide gel electrophoresis and transferred to PVDF membranes, which were subsequently blocked with 5% skim powdered milk for 2 h on the shaker table, incubated with the relevant primary antibodies (CD9, CD63, EpCAM, TSG101 and Calnexin) at 4 °C overnight, and then incubated with secondary antibodies at room temperature for 2 h. An ECL kit was used to detect the bands.

2.18. EV-ber uptake in vitro and in vivo

To investigate the internalization of EV-ber in LLC cells, recipient cells were cultured on coverslips in a 24-well plate and labeled with the fluorescent dye PKH26. DiO-labeled EV-ber was then added to the wells and incubated. After 1, 6, and 24 h, the medium was removed, and the cells were gently washed with PBS. Subsequently, the coverslips were mounted onto slides and further stained with DAPI. Cellular uptake was then visualized using immunofluorescence microscopy. For quantitative assessment of cellular uptake, DiO-labeled EV-ber was introduced to unstained recipient cells. At 1, 6, and 24 h post-incubation, the percentage of DiO-positive cells was analyzed by flow cytometry to evaluate EV-ber uptake. Flow cytometry experiments were performed in triplicate.

Approximately 60 μg of DiR-labeled EV-ber in 100 μL of PBS was administered individually to mice bearing subcutaneous LLC tumors *via* gavage (i.g.), tail vein injection (i.v.), or intraperitoneal injection (i.p.). After 6 and 24 h, bioluminescence imaging was performed using excitation/emission wavelengths of 750 nm/790 nm (In Vivo Xtreme, Bruker, Germany) to track the distribution of EV-ber *in vivo*. The biodistribution of liposomes and MSC-EVs was monitored under the same imaging conditions.

2.19. Live/dead cell co-staining assay

LLC and H1975 cells were grown on coverslips in 24-well plates overnight with 70% density. Then they were treated with PBS, 1.2 μg/mL Ber which was same with the drug content in EV-ber, 40 μg/mL (100 μmol/L) Ber, 60 μg/mL EV-ctrl and 60 μg/mL EV-ber, respectively. After 48 h incubation, initial medium was discarded and cells were washed with PBS gently. Then, the 1000 × calcein AM and PI in buffer were added into the plate and incubated with cells for 1 h. Then coverslips were taken out to be observed under immunofluorescence microscope as soon as possible. The number of live/dead cells were counted by ImageJ (Fiji, NIH, MD, USA).

2.20. Mouse experiments

2.20.1. Subcutaneous tumor model

5×10^5 LLC cells in 100 μL FBS-free DMEM medium were injected subcutaneously into the right axilla of 6-week-old female C57BL/6 mice (Hubei biont bio-technology Co., Ltd., Wuhan, China). Mice were raised in specific pathogen free environment in the Wuhan Laboratory Animal Center of Tongji Medical College with permission of Animal Care and Use Committee of Tongji Medical College. They were randomized into 5 groups ($n = 5$ or 6 in each group): a. 100 μL PBS, b. 0.12 mg/kg Ber in 100 μL PBS, c. 3 mg/kg EV-ctrl in 100 μL PBS, d. 5 mg/kg Ber in 10 μL DMSO + 40 μL PEG300 + 5 μL Tween-80 + 45 μL PBS, e. 3 mg/kg EV-ber in 100 μL PBS. For all kinds of treatment, mice were intraperitoneally injected every other day. Tumor growth and body weight were recorded once every two days. Tumor volume was calculated by Eq. (2):

$$\text{Tumor volume} = \text{Length} \times \text{Width}^2 \times 0.5 \quad (2)$$

When subcutaneous tumor volumes reached approximately 30−40 mm^3 for around 7 days, the treatments started. When the tumor volume was over 2000 mm^3, tumor longest diameter exceeded 20 mm, or the body weight decreased by 20%, mice were humanely sacrificed and final tumor volume and body weight were estimated. Serum and different tissues, including tumor, lung, liver, spleen, kidney and heart, were collected for subsequent tests.

For building intratumoral bacteria-removed model (ABTx), mice were injected intravenously with 300 μL ATBx antibiotics suspension (vancomycin (10 mg/mL), imipenem (4 mg/mL), neomycin (1.5 mg/mL)) every 48 h until 48 h before the final analysis end point[5]. For bacterial colonization of tumors, when the tumor volume reached about 30−40 mm^3, the mice were intratumorally injected with 100 μL of 5×10^6 CFU/mL bacteria for one time, and then tumor volume and mice status were observed every other day[26]. At the endpoint, mice were humanely sacrificed and tumors were collected for FCM test. For anti-PD-L1 immunotherapy, mice were intraperitoneally injected with 100 μg anti-PD-L1 antibody every other day, and three injections were administered throughout the treatment period.

2.20.2. Metastasis model

5×10^5 LLC-GFP cells in 100 μL FBS-free DMEM medium were injected subcutaneously into the right axilla of 6-week-old female

C57BL/6 mice. The raise environment and treatments were same to the above. At the termination day, tumor tissue was collected and prepared as single-cell suspension (as described below). Then, fluorescence-activated cell sorting (MA900, SONY, Japan) was conducted for sorting LLC-GFP cells. 50 μL FBS-free DMEM medium containing 5×10^5 sorted LLC-GFP cells (for per mouse) was injected into the tail veins of another batch of 6-week-old female C57BL/6 mice. After 3 weeks, the metastasis was detected by *in vivo* living imaging system, and then the lungs were collected for HE staining.

2.21. Histology analysis

Mouse tumor, heart, lung, liver, spleen and kidney tissues were fixed with 10% paraformaldehyde, and sectioned into tissue blocks with a thickness of 5 μm. After routine dehydration, paraffin embedding, and serial sectioning, the paraffin-embedded sections were stained with haematoxylin and eosin (HE). The sections were scanned by scanner (Pannoramic SCAN, 3DHISTECH, Hungary). The severity of the lung injury was graded based on oedema, congestion, neutrophil infiltration, haemorrhage, hyaline membranes and alveolar septal thickening. Liver injury was assessed based on haemorrhage, hepatocyte necrosis, inflammatory cell infiltration, cytoplasm vacuolization and nuclear condensation. Lung metastasis area was analyzed by ImageJ (NIH).

2.22. Immunohistochemistry and immunofluorescence

Immunohistochemical analyses were performed using a standard protocol detailed previously[27]. Antigens were retrieved in EDTA (pH 9) buffer. Then 3% hydrogen peroxide was applied to block endogenous peroxidase. Primary antibodies were incubated overnight on 4 °C, followed with secondary antibodies incubation. Positive cells were visualized using a 3,3′ diaminobenzidine (DAB) substrate. Mouse or rabbit control IgGs were used as negative controls. For immunofluorescence, sections were stained with Alexa 488, Cy3 or Cy5-labeled secondary antibodies. Nuclei were labeled with 4,6-diamidino-2-phenylindole (DAPI) and images were obtained using a scanner (3DHISTECH). ImageJ (NIH) software was used to analyze the positive area and average OD value of immunohistochemistry images and counts of fluorescent cells in immunofluorescence images.

2.23. TUNEL assay

TUNEL staining was performed to detect apoptotic cells in paraffin-embedded tumor tissue sections according to the manufacturer's protocol. Briefly, tissue sections were deparaffinized in xylene, rehydrated through graded ethanol series, and subjected to antigen retrieval using proteinase K (20 μg/mL, 37 °C, 15 min). After permeabilization with 0.1% Triton X-100 in PBS (10 min, room temperature), sections were incubated with TUNEL reaction mixture (enzyme solution + label solution, 1:9 ratio) for 1 h at 37 °C in a dark humidified chamber. Nuclei were counterstained with DAPI (1 μg/mL, 5 min), and slides were mounted with antifade mounting medium. Apoptotic cells were visualized using a scanner (3DHISTECH). Excitation/emission: 488 nm/530 nm for Tunel signal; 358 nm/461 nm for DAPI.

2.24. Serum analysis

Blood was centrifuged at 3000 rpm for 15 min to collect clear serum and frozen in −80 °C as soon as possible. The serum was used at once. The serum activities of ALT, AST, TBiL and Cr were measured using corresponding reagent kits according to manufactures' instructions.

2.25. Distribution of immune cells in tumor immune environment

To analyze changes of immune cells in tumors, we dissected tumor tissues into about 1 mm fragments and then they were incubated in 3 mL FBS-free DMEM medium containing 2.5 mg/mL collagenase IV for 1 h at 37 °C on the constant temperature shaking table. Then, cells suspensions were filtered through 70-mm nylon mesh followed by once PBS washing, once lysis of red blood cells and twice PBS washing again. Then the single-cell suspensions were underwent stimulating in 1 mL DMEM with 10% FBS and 1 μL Leuko Act Cktl with GolgiPlug in 48-well plate for 5 h at 37 °C with 5% CO_2, followed by blocking Fc receptors by CD16/CD32 and live/dead cell staining by Fixable Viability Stain 510 for 20 min, staining surface antigens for 30 min subsequently, and fixation with permeabilization and staining intracellular/intranuclear antigens lastly. Above all centrifugations were 500 $\times g$ for 5 min and at 4 °C. Eventually, samples were detected by flowcytometry (FACSymphony™ A1, BDbioscience, CA, USA) and analyzed by Flowjo (BDbioscience). The reagents and antibodies are listed in Supporting Information Table S1, and the gating strategies are shown in Supporting Information Fig. S1.

2.26. qPCR quantification

About using qPCR to quantify the content of bacteria in tumor tissue, we utilized Aikun Fu et al.'s[5] protocol with minor modifications. Around 100 mg tumor tissue was used to extract DNA. Tumor tissue samples were grinded in 1 mL sterile PBS. Centrifuge at 13,000$\times g$ for 10 min and discard the supernatant. Total genomic DNA was extracted from tumor tissue with the QIAamp PowerFecal (pro) DNA kit (#51804, QIAGEN, Germany) according to the manufacturer's instructions.

For detecting the specific strains, digital PCR was conducted. Specifically, the extracted DNA samples was detected according to manufacturer's instructions of Tsingke 2 × T5 fast qPCR mix (TSE301, Tsingke, Beijing, China). The primer information was listed in Supporting Information Table S2.

For the total bacteria detecting, V9 region of the 16S ribosomal RNA were amplified with following primers: Forward 5′-CGGTGAATACGTTCYCGG-3′, Reverse 5′-GGWTACCTTGTTACGACTT-3′. *Escherichia coli* DNA was used to plot a standard curve to calculate bacterial DNA concentration in the samples[28]. The qPCR quantification was conducted by Sybergreen PCR kit (Q311-02, Vazyme, Nanjing, China) according to the manufacturer's instructions. Raw threshold cycle (Ct) values were normalized according to a bacterial standard curve produced with *Escherichia_coli* DNA, then the number of V9 copies was calculated.

2.27. 2bRAD-M

2.27.1. Sample collection

All mouse tumor samples were carefully dissected and collected on the lab bench using sterile instruments. Immediately after collection, the samples were quickly stored in liquid nitrogen. For environmental controls, PBS from the same batch used during the procedure was placed in cryogenic tubes and exposed to identical conditions.

2.27.2. Library preparation and sequencing

The 2bRAD-M library preparation closely followed the original protocol by Wang et al.[29], with some adjustments. DNA samples, ranging from 1 pg to 200 ng, were digested with 4 units of BcgI enzyme (NEB) for 3 h at 37 °C. Adaptors were then ligated to the DNA fragments. This ligation process involved mixing 5 μL of digested DNA with 10 μL of a master mix containing 0.2 μmol/L of each adaptor and 800 units of T4 DNA ligase (NEB), incubated at 4 °C for 12 h.

Following ligation, the products were amplified, and the resulting PCR products were separated on an 8% polyacrylamide gel. Fragments around 100 bp were excised from the gel and allowed to diffuse into nuclease-free water at 4 °C for 12 h. Sample-specific barcodes were introduced *via* PCR using platform-specific primers. Each 20 μL PCR reaction included 25 ng of gel-extracted PCR product, 0.2 μmol/L of each primer, 0.3 mmol/L dNTPs, 1 × Phusion HF buffer, and 0.4 units of Phusion high-fidelity DNA polymerase (NEB). After purification using the QIAquick PCR Purification Kit (Qiagen), the libraries were sequenced on the Illumina NovaSeq PE150 platform.

2.27.3. Data analysis and decontamination

2.27.3.1. Identification of species-specific 2bRAD-markers. To develop species-specific 2bRAD-M markers, we first downloaded 173,165 microbial genomes (including bacteria, fungi, and archaea) from the NCBI RefSeq database. Using custom Perl scripts, we simulated the digestion of these genomes with 16 type 2B restriction enzymes, creating a comprehensive 2bRAD microbial genome database. Each set of 2bRAD tags was assigned a GenBank Assembly (GCF) number along with its taxonomic information.

We then identified 2bRAD tags that occurred uniquely within each genome and compared them across all genomes. Tags that were specific to a single species-level taxon (without overlap with any other species) were designated as species-specific 2bRAD markers, forming our final 2bRAD marker database.

For decontamination, we employed the Read Level Decontamination (RLD) method[30]. This involved normalizing (subsampling) the reads from the negative control. The number of sequences to be removed (D) was calculated based on the read counts in both the target sample (T) and the negative control (N) (Eq. (3)):

$$D = N \times \frac{T}{T+N} \tag{3}$$

2.27.3.2. Calculation of relative abundance. To identify microbial species in each sample, we mapped the quality-controlled 2bRAD tags against the 2bRAD marker database, which contained unique tags for 26,163 microbial species. To minimize false positives, a G score (Eq. (4)) was calculated for each identified species, representing a harmonic mean of the read coverage of its 2bRAD markers and the total number of possible markers for that species. A G score threshold of 5 was set to control false discoveries.

$$G\,score_{species\ i} = \sqrt{S_i \times t_i} \tag{4}$$

S is the number of reads assigned to all 2bRAD markers belonging to species i within a sample. T is number of all 2bRAD markers of species i that have been sequenced within a sample.

We then calculated the average read coverage for each species' 2bRAD markers, reflecting the number of individuals of that species present in the sample at a given sequencing depth. Finally, the relative abundance of each species was determined as the ratio of its individuals to the total number of detectable individuals from known species within the sample (Eq. (5)).

$$Relative\ abundance_{species\ i} = \frac{S_i/T_i}{\sum_{i=1}^{n} S_i \Big/ T_i} \tag{5}$$

S is the number of reads assigned to all 2bRAD markers of species i within a sample. T is the number of all theoretical 2bRAD markers of species i.

2.28. Bone marrow-derived dendritic cells (BMDCs), bone marrow-derived macrophages (BMDMs), spleen T cells

Murine BMDCs and BMDMs were generated, as described previously. Mouse bone marrow cells were isolated from the femoral cavity, red blood cells were lysed, and then differentiation culture was carried out. 20 ng/mL granulocyte-macrophage colony-stimulating factor (GM-CSF) and 10 ng/mL interleukin-4 (IL-4) for BMDCs, and 20 ng/mL macrophage colony stimulating factor (M-CSF) for BMDMs were respectively added into RPMI-1640 medium supplemented with 10% FBS, plus 100 μg/mL of penicillin, 100 μg/mL of streptomycin. The antibiotics were removed before cells were cocultured with bacteria.

After the cells obtained by grinding the mouse spleen were lysed to remove red blood cells, $CD3^+$ T cells are obtained by negative selection with magnetic beads. The cells were placed in RPMI-1640 medium containing 10 ng/mL interleukin-2, 10% FBS, 100 μg/mL penicillin, 100 μg/mL streptomycin, 10 mmol/L HEPES buffer, 1 mmol/L sodium pyruvate, and 50 μmol/L 2-mercaptoethanol, and then dispensed into a 48-well plate precoated with anti-CD3 and anti-CD28 antibodies for expansion culture.

For bacteria-cell co-culture, the bacteria were typically added at a ratio of 20:1 cell (multiplicity of infection (MOI) 20)[31].

2.29. Statistical analysis

Statistical analyses were performed using GraphPad Prism (V9.0, GraphPad Software, CA, USA). All data were shown as the mean ± standard error of mean (SEM). For two groups, significance of mean differences was determined using unpaired Student's *t*-test. For multiple groups, one-way ANOVA and further multiple comparisons were carried out with Tukey test or Dunnet T3 test. Kruskal−Wallis test was used when the sample distributions were not normally. Overall survival was calculated with Kaplan−Meier analysis. More details were listed in the relevant figure legends.

3. Results

3.1. Deciphering the tumor-immune-microbe interactions in LUAD

To determine whether there is a distinct microbial distribution among different cells in lung cancer tissues, our research involved analyzing two publicly available datasets (LUAD-Set1 and LUAD-Set2)[13,14], in which the scRNA seq data of 5 LUAD and 5 pared normal lung tissues, respectively, were analyzed. Using CellRanger and Seurat[16] with default parameters, cells were classified into 11 primary clusters of LUAD-Set1 (Fig. 1A, left). Using SAHMI pipeline[15], we identified the microbial signals from single-cell transcriptomic sequencing of host tissues. Among the 533 microbial taxa identified, the distributions of the 34 most abundant taxa across various cell types are presented in Fig. 1A (right panel). Significant differences were observed in the abundances of five bacterial genera: *Lysinibacillus* (*Lys*), *Stenotrophomonas* (*Ste*), *Weissella* (*Wei*), *Comamonas* (*Coma*), and *Aeromonas* (*Aero*) between LUAD and normal tissues. Specifically, *Lys* and *Ste* exhibited higher abundance in LUAD tissues, whereas *Wei*, *Coma*, and *Aero* were more abundant in normal tissues (Fig. 1B). For clarity in discussion, we provisionally classified *Lys* and *Ste* as "harmful bacteria", and *Wei*, *Coma*, and *Aero* as "beneficial bacteria". UMAP plots generated for these bacteria, categorized as either beneficial or harmful, suggested a tendency for "harmful bacteria" to be more prevalent in myeloid cells (Fig. 1C, left), while "beneficial bacteria" appeared more frequently in lymphoid cells (Fig. 1C, right). However, individual cluster plots for these bacteria did not strongly corroborate this trend (Supporting Information Fig. S2A). To determine the relative abundance of these bacterial taxa across different immune cell types, we compared their proportions among all associated bacteria within distinct immune cell populations. In LUAD-Set1, the percentages of *Lys* and *Ste* in macrophages were significantly higher than those in $CD4^+$ T cells and natural killer (NK) cells. *Wei* exhibited significantly higher abundance in $CD8^+$ T cells compared to Treg cells and macrophages, and its percentage in NK cells was also significantly greater than that in Treg cells. *Coma* was significantly more abundant in NK cells than in Treg cells and granulocytes. *Aero* showed significantly higher abundance in $CD8^+$ T cells compared to Treg cells and granulocytes (Fig. 1D). In LUAD-Set2, no significant differences were observed in the distribution of *Lys* across different immune cell populations. *Ste* remained significantly more abundant in macrophages than in $CD8^+$ T cells. *Wei* was significantly enriched in $CD8^+$ T cells compared to myeloid cells. *Coma* was significantly more abundant in NK cells than in macrophages and granulocytes. Aero was also significantly more abundant in $CD8^+$ T cells than in granulocytes (Fig. 1E). It is well known that in the tumor immune microenvironment (TIME), Treg cells, macrophages, and granulocytes are immunosuppressive cells[32,33], while $CD8^+$ T and NK cells are immune-stimulatory cells[34,35].

To determine whether the heterogeneous distribution of bacteria across different cell types influences the tumor immune status, we next investigated whether the presence of these five bacterial taxa was associated with host cell gene expression. Using Wilcoxon testing, bacterial and host cell barcode pairing enabled the identification of differentially expressed genes (DEGs) in cells associated with specific bacteria. The numbers of DEGs in LUAD-Set1 for cells with or without *Lys*, *Ste*, *Wei*, *Coma*, and *Aero* were 21, 48, 75, 21, and 18, respectively, and in LUAD-Set2 were 323, 53, 55, 86, and 36, respectively. Gene Ontology (GO) enrichment analysis was conducted using these DEGs. Overall, cells associated with *Lys* or *Ste* were enriched in signaling pathways related to tumor promotion, including immune suppression, whereas cells associated with *Wei*, *Coma*, or *Aero* were enriched in pathways related to tumor inhibition, including anti-tumor immune activation (Fig. 1F and G). The enrichment pathways of *Lys* and *Ste*-associated cells mainly were the activation and migration of myeloid cells, lipid synthesis, transport, and storage pathways, which were considered to be associated with poor prognosis of tumors[36]. The enrichment pathways of *Wei, Coma* and *Aero*-associated cells mostly were those related to the activation of anti-tumor immunity or the inhibition of tumor cell proliferation, such as antigen presentation, cytotoxic T cell activation, lymphocyte differentiation and the regulation of cell cycle[37]. Thus, we preliminarily inferred that *Lys* and *Ste* might be detrimental to the progression of LUAD, while *Wei*, *Coma*, and *Aero* might be able to suppress LUAD, which was consistent with the existing reports[38−42].

To ultimately clarify the effects of these bacteria on LUAD progression and whether there are consistent factors between homo sapiens and mice, we employed an experiment of directly injecting bacterial suspension into tumors for verification[43]. We selected the species that have been reported to exist in the human body under these five genera for the experiment, namely: *Lysinibacillus_sphaericus* (*L. sphaericus*), *Stenotrophomonas_maltophilia* (*S. maltophilia*), *Weissella_cibaria* (*W. cibaria*), *Comamonas_testosteroni* (*C. testosteroni*), *Aeromonas_veronii* (*A. veronii*), and the abbreviations in the following text are still *Lys*, *Ste*, *Wei*, *Coma*, and *Aero*. Specifically, when the subcutaneous LLC tumor grew to approximately 40 mm^3, 100 μL of PBS containing 5×10^6 bacteria was injected into the tumor, and then the tumor growth volume was monitored (Fig. 1H). Data from quantitative PCR performed on tumor tissues obtained at the end of the experiment demonstrated the successful colonization of bacteria in the tumor tissues (Fig. S2B). Compared with the PBS group, the tumor volume in the *Wei* and *Coma* groups decreased by approximately 1/3 ($P = 0.0273$ and 0.0628, respectively), while which in the *Lys* and *Ste* groups increased significantly (Fig. 1I). During the 10-day growth period after the bacterial injection, the body weight of the mice generally increased without a decrease (Fig. 1J), indicating that such amount of bacterial injection did not cause harm to the mice. At the end, the tumors were removed for multicolor flow cytometry analysis. Although there was no difference in the overall DC percent (Fig. S2C), the percent of mature DC cells (mDCs) in the *Lys*, *Ste*, *Wei*, and *Coma* groups was significantly increased compared with the control group (Fig. S2D), which may be due to the stimulating effect of bacteria on DC cells within the tumor. The total T cell percent in the *Wei* group was significantly higher than that in PBS group, with lower T cell percent in the *Lys* and *Ste* groups (Fig. 1K), and the total $CD4^+$ T cell percent was significantly lower than that in the control, *Lys* and *Aero* group (Fig. S2E). It is worth noting that the total T cells in the *Aero* group showed a downward trend. Although there was no difference in the total $CD8^+$ T cell percent (Fig. S2F), the percent of $CD69^+CD8^+$ T cells (meaning activated $CD8^+$ T cells) in the *Wei* group and the *Coma* group was significantly higher than that in controls, while the *Lys* and *Ste* groups had significantly contrast trend (Fig. 1L). The percent of Treg cells in *Wei* and *Coma* groups was significantly lower than that in other groups (Fig. 1M). Compared with the PBS group, the overall macrophage cells (TAMs) percent in the *Wei* group decreased

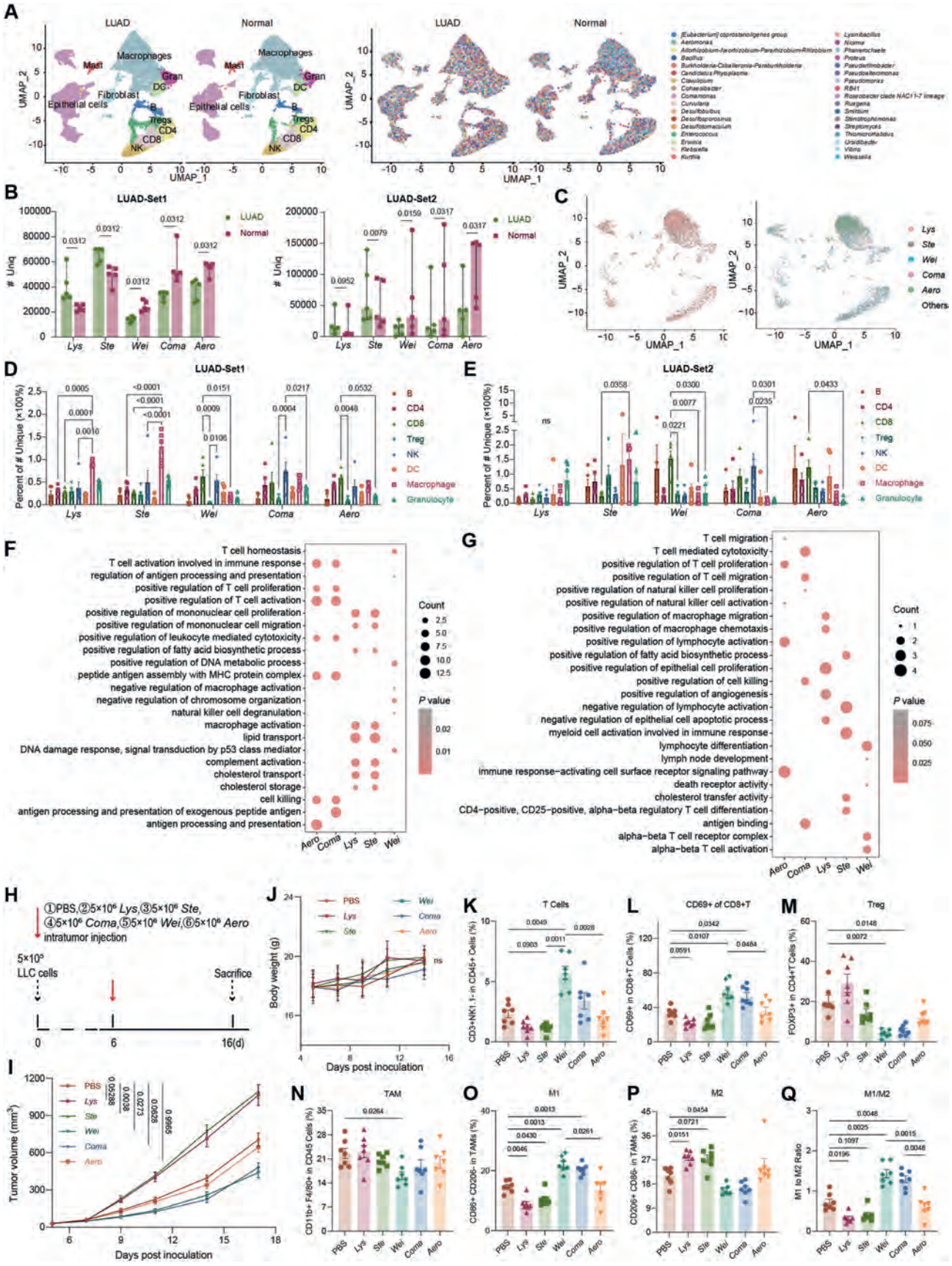

Figure 1 Deciphering the Tumor-Immune-Microbe interactions in lung adenocarcinoma. (A) (left) UMAP plots showing the host somatic cells of LUAD (n = 70,998 cells) and normal tissues (n = 57,563 cells) in LUAD-Set1, and (right) the distribution of top 34 microbial taxa (at genus

significantly (Fig. 1N), and the percent of M1-type macrophages in *Wei* and *Coma* groups increased significantly, and decreased significantly in *Lys* and *Ste* groups (Fig. 1O), while the percent of M2-type cells showed a basically consistent reverse change (Fig. 1P). Thus, the *Lys* and *Ste* groups had lower M1/M2 ratios, and the *Wei* and *Coma* groups had the higher ones (Fig. 1Q). There was no meaningful change in the percent of NK cells and NKT cells between groups (Fig. S2G and S2H). Overall, in mice, *Lys* and *Ste* played an inhibitory role in the TIME, thereby promoting LUAD progression, while *Wei* and *Coma* played a promoting role in the TIME, thereby inhibiting LUAD progression, which is relatively consistent with the results in humans mentioned above; however, the immune-promoting and LUAD-inhibiting effects of *Aero* in mice were not manifested.

3.2. Identification of berberine as the preferred microbiome modulator through drug screening

Based on the above data, we identified two tumor-promoting bacterial species (*Lys* and *Ste*) and two tumor-suppressing species (*Wei* and *Coma*). However, direct administration of live bacteria into the body as a therapeutic approach poses potential safety concerns. Therefore, we sought to identify safe and effective compounds capable of selectively eliminating tumor-promoting bacteria while promoting the growth of tumor-suppressing bacteria, thereby mimicking the functional roles of the beneficial bacteria. To achieve this, we screened a compound library consisting of 281 compounds with both antibacterial and anti-tumor properties using *in vitro* assays. When *Lys*, *Ste*, *Wei*, and *Coma* reached their logarithmic growth phase, they were seeded into 96-well plates at a density of 1×10^5 CFU per well, and 0.1 mmol/L of each compound was added. 1% DMSO and 50% DMSO were used as negative and positive controls, respectively. After incubation for 12−16 h, the absorbance at 600 nm was measured to assess bacterial viability (Fig. 2A). The Z score for each plate ranged between 0.5 and 1.0, indicating reliable assay performance (Supporting Information Fig. S3A). Fig. 2B illustrates the effects of all tested compounds on the viability of the four bacterial species. A relative viability of less than 25% was defined as the threshold for growth inhibition, while a relative viability exceeding 100% was considered indicative of bacterial growth stimulation. We identified the common intersection among the compound sets: 97 compounds that inhibited *Lys*, 33 that inhibited *Ste*, 58 that stimulated *Coma*, and 152 that stimulated *Wei*[44] (Fig. 2C). Finally, two intersection compounds were obtained, namely berberine and vancomycin. After retrieving the data of these two compounds, the high frequency of vancomycin causing ototoxicity and nephrotoxicity is a cause for concern[45,46], therefore vancomycin was excluded. Next, we focused our research on berberine. We re-verified the effects of berberine on the growth of the four bacteria and found that it showed dose-dependent inhibition of *Lys* and *Ste*, with IC_{50} values of 0.02315 and 0.02894 mmol/L, respectively, while the stimulating growth effect on *Wei* and *Coma* was still obvious at different concentrations (Fig. 2D).

After studying the antibacterial effect of berberine (Ber), its anti-LUAD effect was explored. CCK-8 results demonstrated that Ber effectively inhibited the proliferation of lung adenocarcinoma cells in a dose-dependent manner. The IC_{50} values of Ber on LLC, H1975, H1299, and A549 cells were determined to be 66.69, 28.63, 38.74, and 46.00 μmol/L, respectively (Fig. 2E), which were less than those on *Lys* and *Ste*. When the H1299, A549, H1975, and LLC cell lines were stimulated with 40 μmol/L and 80 μmol/L Ber (the concentration was obtained with reference to the IC_{50} value), the cell colony formation ability was significantly weakened, and this weakening effect was already very significant at a concentration of 40 μmol/L (Fig. S3B, Fig. 2F). Then, we examined whether berberine would cause apoptosis in LUAD cell lines. Using flow cytometry, we found that after the H1299, H1975, and LLC cell lines were stimulated with 40 μmol/L and 80 μmol/L berberine for 48 h, the proportion of apoptotic cells increased significantly, but the proportion of apoptotic cells in HBE did not exceed 10%, suggesting a mild cytotoxic effect on normal lung epithelial cells (Fig. S3C, Fig. 2G). Furthermore, the *in vivo* anti-tumor effect of berberine was investigated. Previous study has shown that the bioavailability of berberine through intraperitoneal route was much better than through oral/intragastric route[47]. Thus mice with LLC-subcutaneous tumors were treated with intraperitoneal injection of 5 mg/kg Ber (determined by previous research[48]) every other day. At the end of the observation (the 13th day of tumor-bearing), the tumor volume of the treatment group mice was reduced by more than 40% compared with the control group ($P = 0.043$) (Fig. 2H), and the body weight did not decrease (Fig. 2I). Overall, berberine, a microbiota modulator obtained through high-throughput compound screening based on tumor-promoting bacteria and tumor-suppressing bacteria, also has the potential to resist LUAD *in vitro* and *in vivo*.

3.3. Synthesis and characteristics of tumor cell-derived extracellular vesicles loading berberine

The low solubility of berberine (less than 2.57 mmol/L in water and less than 25 mmol/L in DMSO) may limit its efficacy at therapeutically relevant concentrations *in vivo*. To address this limitation, we aimed to identify a suitable biological carrier for encapsulating berberine. In our previous studies, methotrexate and fluvastatin were successfully loaded into tumor cell-derived microparticles (TMPs) using a natural incubation method, thereby enhancing the bioavailability of these drugs[20,21]. *In vivo* imaging data from mice bearing subcutaneous LLC tumors demonstrated

level) among cell clusters in LUAD and normal tissues ($n = 5$). (B) The Uniq counts of *Lys*, *Ste*, *Wei*, *Coma* and *Aero* in LUAD and normal tissues ($n = 5$). Median and 95% confidence interval (95% CI) are shown, Wilcoxon. (C) UMAP plots of the distribution of *Lys*-*Ste*-others (left) and *Wei*-*Coma*-*Aero*-others (right) among cell clusters in LUAD and normal tissues ($n = 5$), LUAD-Set1. The percents of Uniq counts of *Lys*, *Ste*, *Wei*, *Coma* and *Aero* of 9 immune cell clusters in LUAD-Set1 (D) and LUAD-Set2 (E), $n = 5$, ANOVA and Tukey test. Dot plots showing the pathways enriched by the DEGs of cells with or without *Lys*, *Ste*, *Wei*, *Coma* and *Aero* in LUAD-Set1 (F) and LUAD-Set2 (G). Dots are size-scaled by P value. Data are shown for pathways with FDR-corrected $P < 0.05$ (Benjamini-Hochberg test). (H) Illustration of bacteria interventions *in vivo* study. (I) The mean tumor volumes of mice with LLC-subcutaneous tumor in groups during observation ($n = 7$). (J) The mean body weights of tumor-bearing mice in groups during observation ($n = 7$). (K−Q) Flow cytometry analyzing the percents of T cells (K), $CD69^+CD8^+$ T cells (L), Treg cells (M), TAMs (N), M1-type TAMs (O), M2-type TAMs (P) and ratio of M1/M2 (Q) in tumors by groups ($n = 7$). ANOVA and Tukey test. Mean ± SEM and P values are shown. ns, not significant.

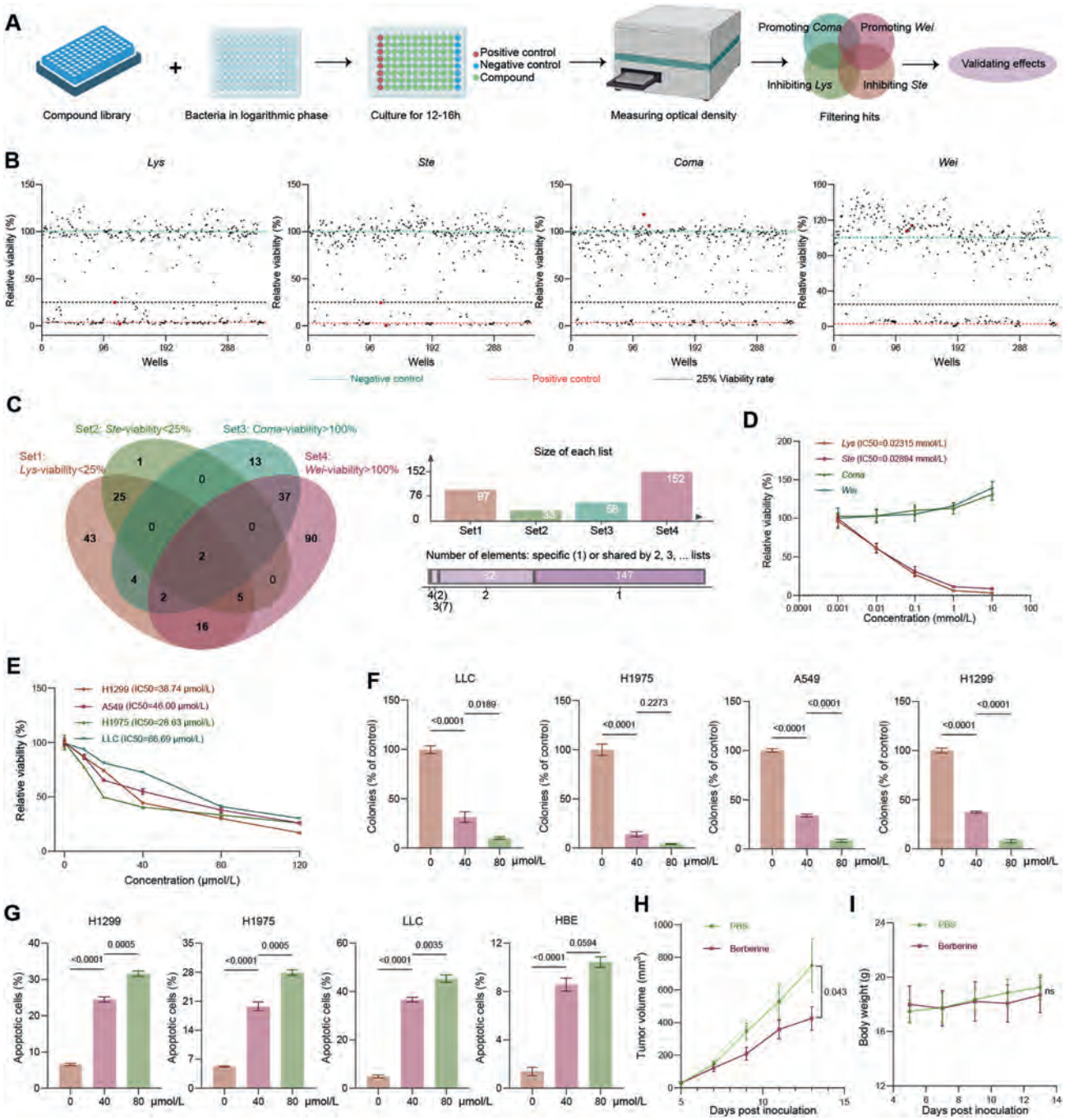

Figure 2 Identification of berberine as the preferred microbiota modulator through drug screening. (A) Illustration of drug screening study. (B) Scatter diagrams showing the relative viability of *Lys*, *Ste*, *Coma* and *Wei* with 0.1 mmol/L compound library stimulation. (C) Venn diagram showing the overlapping relationships of the four sets of compounds that inhibit *Lys*, inhibit *Ste*, stimulate *Coma*, and stimulate *Wei*. (D) The relative viability of *Lys*, *Ste*, *Coma* and *Wei* with the stimulation of multiple specific concentration-Ber ($n = 8$ for per concentration). The IC_{50} values are shown. (E) The relative viability of *Lys*, *Ste*, *Coma* and *Wei* with the stimulation of multiple concentration-Ber ($n = 3$ for per concentration). The IC_{50} values are shown. (F) The colony counts of H1299, A549, H1975 and LLC cells with the stimulation of 0, 40 and 80 μmol/L Ber ($n = 3$). ANOVA and Tukey test. (G) The proportions of apoptotic LLC, H1975, H1299 and HBE cells with the stimulation of 0, 40 and 80 μmol/L Ber for 48 h ($n = 3$). ANOVA and Tukey test. (H, I) The mean tumor volumes (H) and mean body weights (I) of mice with LLC-subcutaneous tumor in PBS and Ber (5 mg/kg, i.p.) group during observation ($n = 10$). Student's *t*-test. Mean ± SEM and *P* values are shown. ns, not significant.

that the tumor tissue-targeting ability of LLC-derived extracellular vesicles (LLC-EVs) was approximately twice that of liposomes and mesenchymal stem cell-derived EVs (MSC-EVs) ($P < 0.05$) (Supporting Information Fig. S4A and S4B). Based on this finding, we selected LLC-EVs as a biological carrier for berberine encapsulation. However, due to the low solubility of berberine,

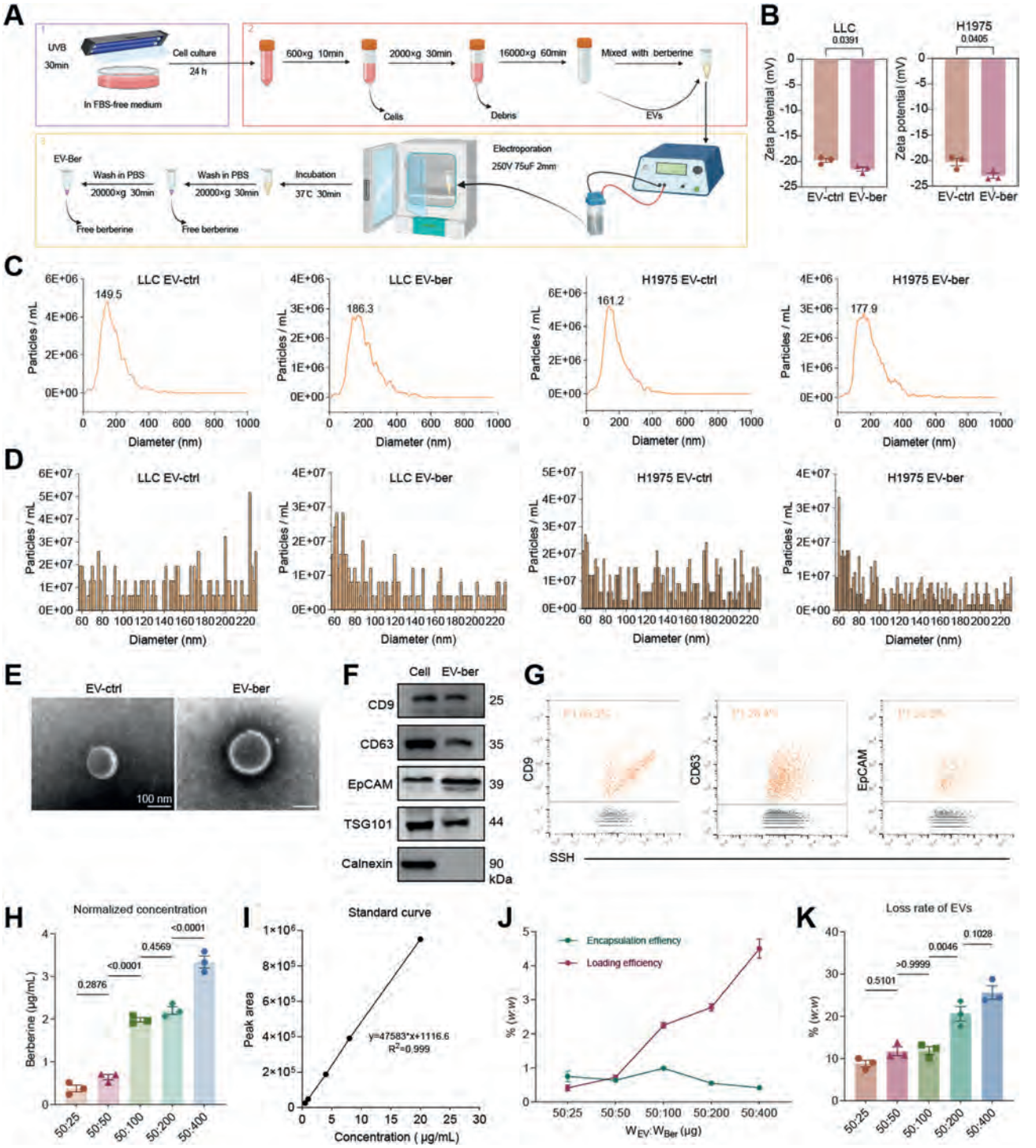

Figure 3 Synthesis and characteristics of tumor cell-derived extracellular vesicles loading berberine. (A) Illustration for fabrication of EV-ber. (B) The zeta potential of EV-ctrl and EV-ber. $n = 3$, Student's t test. The size distribution of EV-ctrl and EV-ber by NTA (C) and RPS (D). (E) The irregular spherical or cup-shaped morphology of EV-ctrl (left) and EV-ber (right) observed by TEM. (F) The positive and negative EV markers expression of LLC cells and EV-ber by Western-blot analysis. (G) The expression of CD9, CD63 and EpCAM on LLC EV-ber analyzed by nFCM. (H) The normalized concentration of berberine in LLC EV-ber at different ratio of W_{EV}:W_{Ber} (μg), detected by HPLC. $n = 3$, ANOVA and Tukey test. (I) The standard curve of peak area between various concentrations of berberine by HPLC detection. (J) The encapsulation efficiency and loading efficiency of LLC EV-ber. (K) The loss rate of EVs at different ratio of W_{EV}:W_{Ber} (μg). Mean ± SEM and P values are shown.

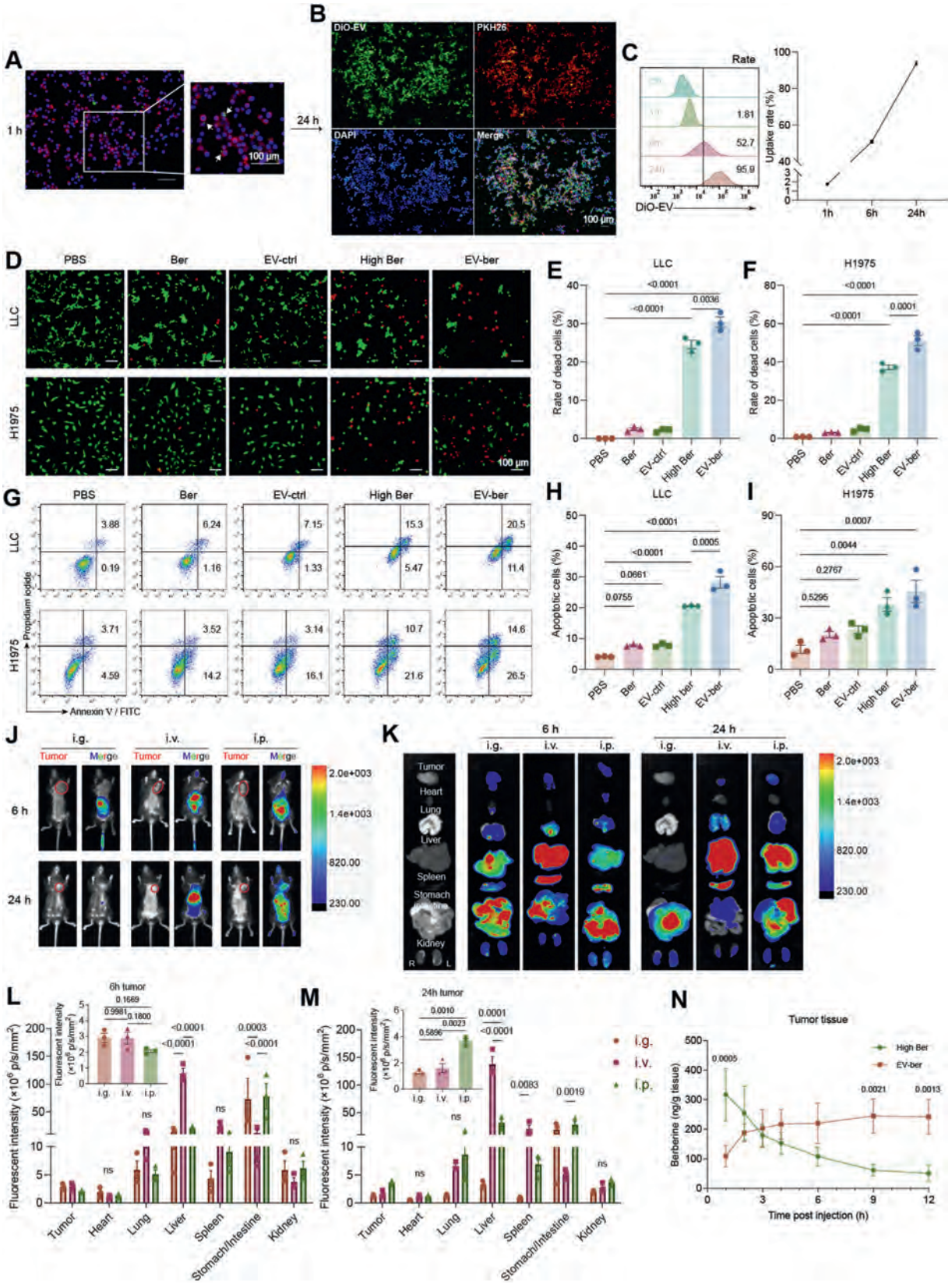

Figure 4 Evaluation of EV-ber uptake efficiency, cytotoxicity *in vitro*, and biodistribution *in vivo*. LLC pre-treated with red membrane dye PKH26 and EV-ber with green fluorescent dye DiO were incubated together for 1 h (A) and 24 h (B). (C) The internalization of EV-ber pre-dyeing with DiO after co-culture with 1×10^5 LLC cells for 1, 6, and 24 h, as measured by flow cytometry. $n = 3$. (D) The representative images of LLC and H1975 live/dead cells with stimulations of PBS, ~1.2 μg/mL Ber, 60 μg/mL EV-ctrl, 38.983 μg/mL High Ber or 60 μg/mL EV-ber for 48 h.

conventional methods such as natural incubation and ultrasonication failed to load it into LLC-EVs. Therefore, we employed electroporation as an alternative loading strategy (Fig. 3A). Following resuspension, the final product exhibited a yellow colloidal appearance (Fig. S4C, right), distinct from the empty EVs (EV-ctrl) (Fig. S4C, left), which may indicate successful berberine incorporation. Subsequently, a range of techniques were utilized to characterize the resulting formulations. The zeta potential of EV-ber was slightly lower than that of EV-ctrl (Fig. 3B). NTA method revealed that the peak diameter of LLC EV-ctrl and H1975 EV-ctrl was 149.5 and 161.2 nm, respectively, while LLC EV-ber and H1975 EV-ber exhibited a slightly larger diameter of 186.3 nm and 177.9 nm, respectively (Fig. 3C). For the same samples, the particle size distribution range measured by RPS method was smaller (less than 230 nm), which may be due to the stronger sensitivity of the RPS method for detecting small particle sizes (Fig. 3D). TEM images manifested the irregular spherical or cup-shaped morphology of both EV-ctrl and EV-ber, with sizes consistent with the NTA and RPS data (Fig. 3E). Additionally, western blotting analysis demonstrated the presence of four classic markers for tumor cell-derived EVs, namely CD9, CD63, EpCAM, and tumor susceptibility gene 101 protein (TSG101), on EV-ber, indicating the retention of parent cell characteristics after processing steps (Fig. 3F). The absence of calnexin protein on EV-ber indicated that EV-ber had good purity (Fig. 3F). Nano flow cytometry analysis also revealed the expression of CD9, CD63 and EpCAM on EV-ber (Fig. 3G).

HPLC was conducted to determine the precise content of berberine in EV-ber. Encapsulation efficiency (EE), defined as the weight of berberine in EV-ber (*W*)/the primary weight of Ber (W_{Ber}), and loading efficiency (LE, defined as *W*/the final weight of EVs (W_{EV})) were utilized to assess the synthesis efficiency. The mean concentration of berberine was determined to be 0.375, 0.640, 1.983, 2.203, and 3.339 μg/mL, when the W_{EV}:W_{Ber} ratio was 50:25, 50:50, 50:100, 50:200 and 50:400, respectively (Fig. 3H), based on the standard curve (Fig. 3I). Although the LE increased with the increasing amount of berberine added to the system, the EE decreased significantly (Fig. 3J) and the loss rate of EVs increased significantly (Fig. 3K). For the economic reasons, the ratio of 50:100 (W_{EV}:W_{ber}) was selected subsequently, which was with a moderate LE, the highest EE, and less EV loss.

Together, these results suggest the successful synthesis of EV-ber that incorporates a specific amount of berberine, along with retaining the classic characteristics of EVs. Additionally, we determined the optimal W_{EV}:W_{Ber} ratio for subsequent synthesis of EV-ber.

3.4. Evaluation of EV-ber uptake efficiency, cytotoxicity in vitro, and biodistribution in vivo

Then, we evaluated the uptake efficiency and biocompatibility of EV-ber *in vitro* and *in vivo*. 1×10^5 LLC cells were labeled with DAPI and PKH26 to mark the cell nucleus and cytomembrane, respectively, and then incubated with 60 μg of DiO-labeled EV-ber. After 1 h of incubation, only a few green granular EVs were observed surrounding the LLC cells (Fig. 4A). However, after 24 h of incubation, the cell membranes were completely stained with green fluorescence (Fig. 4B), indicating that all LLC cells had merged with EV-ber. To determine the uptake rate accurately, flow cytometry was used to detect the positive cells stained with green fluorescence from DiO-labeled EV-ber. As shown in Fig. 4C, the mean positive rate at 1, 6, and 24 h was 1.81%, 52.7%, and 95.9%, respectively. These *in vitro* results indicated that EVs could effectively merge with cytomembranes and deliver drugs into cells. Furthermore, the results suggested that 60 μg EV could merge with 1×10^5 cells after 24 h of co-incubation, indicating that subsequent cytotoxicity analysis should be performed after at least 24 h.

Subsequently, we evaluated the cytotoxic effects of EV-ber on LLC and H1975 cells. Live/dead cell fluorescent staining and flow cytometry were performed to analyze apoptosis in groups treated with PBS, 60 μg/mL EV-ber, 60 μg/mL EV-ctrl, a routine dose (100 μmol/L ~ 38.983 μg/mL, approximately double the IC_{50} value) of free berberine (High Ber), and an equivalent amount (∼1.2 μg/mL) of berberine encapsulated within EV-ber (Ber). The live/dead cell fluorescent staining results demonstrated that in both LLC and H1975 cells, the number of dead cells in the High Ber and EV-ber groups was significantly higher than in the PBS, Ber, and EV-ctrl groups (Fig. 4D−F). Similarly, the apoptosis rates in the High Ber and EV-ber groups were markedly increased, which was consistent with the live/dead staining results (Fig. 4G−I). These findings further confirm the successful preparation of EV-ber and the preservation of the antitumor activity of the encapsulated berberine. Importantly, the EV-ctrl group showed minimal cytotoxicity. Due to the high cellular uptake efficiency of EVs, only 1/40 of the free berberine dose delivered *via* EVs was sufficient to induce an equivalent or even greater cytotoxic effect compared to free berberine alone, highlighting the significant advantage of EVs as drug delivery vehicles.

Next, to investigate the *in vivo* biodistribution of EV-ber, 60 μg of DiR-labeled EV-ber was administered to mice bearing subcutaneous LLC tumors *via* gavage (i.g.), tail vein injection (i.v.), and intraperitoneal injection (i.p.), respectively, followed by *in vivo* imaging. *In vivo* imaging data showed that at 6 h post administration, fluorescence in all three groups was predominantly localized in the abdominal region, including the liver, digestive tract, spleen, and kidneys. At 24 h post-administration, fluorescence in the i.g. group had largely dissipated, whereas in the i.v. and i.p. groups, fluorescence not only remained in the abdominal organs but also began to accumulate in the thoracic region (lungs) and tumor sites (Fig. 4J). Images of *ex vivo* organs further demonstrated that at 6 h post-administration, the i.v. group exhibited the strongest fluorescence in the liver and spleen, with relatively strong signals in the lungs. In contrast, in the i.g. and i.p. groups, the most intense fluorescence was observed in the gastrointestinal tract. There was minimal variation in fluorescence

Green represents live cells and red represents dead cells. The ratio of LLC (E) and H1975 (F) dead cells. $n = 3$, ANOVA and Tukey test. (G) The representative gating images of flow cytometry for apoptosis analysis. The apoptosis rate of LLC (H) and H1975 (I) cells with stimulations of PBS, ∼1.2 μg/mL Ber, 60 μg/mL EV-ctrl, 38.983 μg/mL High Ber or 60 μg/mL EV-ber for 48 h ($n = 3$). ANOVA and Tukey test. The representative images of the accumulation of DiR-labelled EV-ber *in vivo* (J) and *ex vivo* organs (K) at 6 and 24 h post i.g., i.v., and i.p. administration. The radiant efficiency results of vital organs at 6 h (L) and 24 h (M) post administration ($n = 3$ per time point). (N) The concentration of berberine in tumor tissue post intraperitoneally injecting 5 mg/kg berberine and 60 μg EV-ber, by HPLC analysis ($n = 3$ per time point). ANOVA and Tukey test. Mean ± SEM and *P* values are shown. ns, not significant.

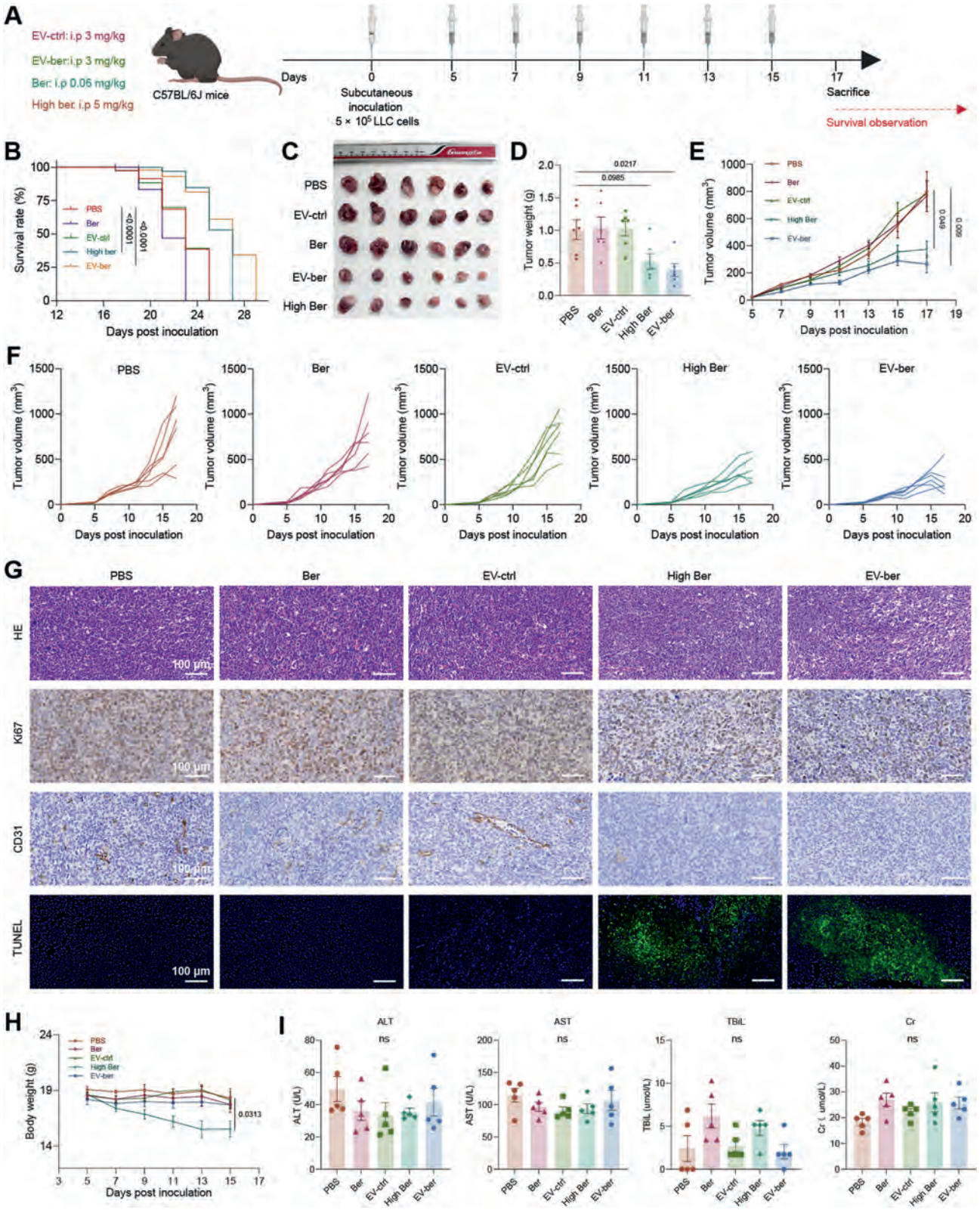

Figure 5 Evaluation of safety and anti-LUAD effect of EV-ber *in vivo*. (A) The schematic illustration for treatments after subcutaneous tumor models were built. (B) The kaplan−Meier curves showing the survival rates of C57 mice bearing LLC-subcutaneous tumor with the treatments of PBS, 0.06 mg/kg Ber, 3 mg/kg EV-ctrl, 5 mg/kg High Ber or 3 mg/kg EV-ber ($n = 8$). Mantel−Cox test. The survival endpoints including: natural death, tumor volume exceeding 2000 mm^3, tumor longest diameter exceeding 20 mm, or body weight loss exceeding 20%. The appearance of tumors (C), mean naked tumor weight (D) and mean tumor volume (E) of C57 mice bearing LLC-subcutaneous tumor ($n = 6$) with the treatments of PBS, 0.06 mg/kg Ber, 3 mg/kg EV-ctrl, 5 mg/kg High Ber or 3 mg/kg EV-ber for 12 days. ANOVA and Tukey test. (F) The tumor growth curves

intensity in other organs among the three groups (Fig. 4K and L). At 24 h post-administration, fluorescence in the i.g. group was detected only in the liver and kidneys. In the i.v. group, fluorescence remained concentrated in the liver, spleen, and lungs. In contrast, in the i.p. group, fluorescence was observed not only in the liver, spleen, gastrointestinal tract, and lungs, but also showed a more pronounced accumulation at the tumor site compared to the other two groups (Fig. 4K and M). These findings indicate that intraperitoneal administration is more effective for tumor targeting than gavage or intravenous administration. This enhanced targeting may be attributed to the shorter retention time of EV-ber in the liver and lungs, thereby reducing clearance by the mononuclear phagocyte system. Furthermore, the drug content in tumor tissues following i.p. injection of 5 mg/kg free berberine (High Ber) and 60 μg EV-ber was quantified by HPLC. The High Ber group exhibited a time-dependent decrease in drug concentration, whereas the EV-ber group showed a gradual increase in drug content over time. At 9 and 12 h post administration, the tissue drug concentration in the EV-ber group was nearly four times higher than that in the High Ber group ($P < 0.05$; Fig. 4N), further confirming that EV-ber effectively delivers berberine to the tumor site. In conclusion, EV-ber demonstrates superior tumor-targeting capability *in vivo*, and intraperitoneal injection is more effective than gavage or intravenous injection for achieving this.

3.5. Evaluation of safety and anti-LUAD effect of EV-ber in vivo

Next, we evaluated the *in vivo* anti-LUAD efficacy of EV-ber. Mice were randomly assigned to five treatment groups once the volume of LLC-subcutaneous tumors reached approximately 30 mm^3. The therapeutic dose and route of administration for free berberine were consistent with the previous experiment: 5 mg/kg *via* intraperitoneal injection (High Ber group). Mice in the EV-ctrl and EV-ber groups received 3 mg/kg of EVs, with the corresponding berberine content in EV-ber calculated as 0.06 mg/kg based on HPLC analysis (Ber group) (Fig. 5A). The median survival times of mice treated with PBS, EV-ctrl, Ber, High Ber, and EV-ber were 23, 23, 21, 27, and 27 days, respectively (Fig. 5B). The overall log-rank test indicated a significant difference in survival among the five groups ($P < 0.0001$), and the Mantel-Cox test revealed statistically significant differences between the PBS group and both the EV-ber group and the High Ber group ($P < 0.0001$). Another independent experiment demonstrated that after five treatment cycles, significant differences in tumor size were observed among the groups (Fig. 5C). Specifically, the average tumor weight in the EV-ber group was significantly lower than that in the PBS, EV-ctrl, and Ber groups (Fig. 5D). Moreover, tumor volumes in both the High Ber and EV-ber groups were reduced by more than 50% compared to the PBS, EV-ctrl, and Ber groups (Fig. 5E and F). To further elucidate the mechanisms underlying EV-ber-mediated tumor suppression, we performed histopathological analyses, including HE staining, proliferation index assessment, microvessel density evaluation, and TUNEL assay on tumor tissues from all five groups. Paraffin-embedded sections were immunostained with anti-Ki67 and anti-CD31 antibodies to assess tumor cell proliferation and microvessel density, respectively, while the TUNEL assay was used to detect apoptotic cells. HE staining revealed that in the High Ber and EV-ber treated groups, the nuclear size of tumor cells was reduced, nuclear staining became less intense, the cytoplasm-to-nucleus ratio increased, and eosin staining appeared more uniform. Furthermore, both tumor cell proliferation and microvessel density were decreased, while the number of apoptotic cells was increased in the High Ber and EV-ber groups (Fig. 5G).

Meanwhile, we assessed the safety profile of EV-ber treatment. The body weight of mice in the EV-ber group remained stable, whereas the body weight of mice in the High Ber group exhibited a statistically significant continuous decline (Fig. 5H). This observation was inconsistent with the results from the previous experiment (Fig. 2I). We hypothesized that this might be caused by chronic abdominal inflammation induced by the co-solvent present in the High Ber solution following repeated intraperitoneal injections. The use of the co-solvent was necessitated by the low water solubility of berberine. The discrepancy in body weight changes between the two experiments suggests that the safety of free berberine treatment remains uncertain. However, by the end of the intervention period, the observed weight loss did not appear to impair organ function. Specifically, serum levels of ALT, AST, TBiL, and Cr were comparable across all five groups (Fig. 5I), indicating that liver and kidney functions were not adversely affected by any of the treatments. Histopathological examination of the heart, liver, spleen, lungs, and kidneys postmortem revealed no morphological abnormalities in any of the treatment groups (Supporting Information Fig. S5A).

Overall, in mice, a 40-fold higher dose of free berberine is required to achieve an anti-LUAD effect equivalent to that of EV-ber. However, the safety of such a high dose of free berberine remains uncertain, highlighting the safety advantage of EV-ber due to its efficient tumor-targeting capability.

3.6. EV-ber reshapes tumor immune microenvironment and activates adaptive immune responses

Previous studies have demonstrated that berberine could activate $CD8^+$ T cells and repolarize M2-type TAMs into inflammatory M1-type TAMs[48,49]. Therefore, we were encouraged to thoroughly investigate the role of sole berberine and EV-ber in reshaping TIME, including both the adaptive and innate immunity.

T cells, especially $CD8^+$ T cells, are the core effector cells for anti-tumor immunity[34]. Therefore, we first examined the distribution and content of T cells, $CD4^+$ T cells, and $CD8^+$ T cells in the LLC- subcutaneous tumors of mice treated with PBS, Ber, EV-Ctrl, High ber, or EV-ber for 12 days (Fig. 6A). We found that both $CD4^+$ cells and $CD8^+$ cells in the High Ber and EV-ber groups were significantly increased compared with the control groups (Fig. 6B). Then, we leveraged multicolor flow cytometry to more comprehensively and accurately evaluate the effects of berberine and EV-ber on the immune microenvironment. The

of tumor-bearing mice in the five groups. (G) The images of HE staining, immunohistochemistry staining of Ki67 and CD31, and TUNEL assay in tumor tissue. Green for apoptotic cell in TUNEL assay. (H) The mean body weight of the tumor-bearing mice receiving PBS, 0.06 mg/kg Ber, 3 mg/kg EV-ctrl, 5 mg/kg High Ber or 3 mg/kg EV-ber treatments for 12 days. $n = 6$, ANOVA and Tukey test. (I) The serum level of ALT, AST, TBiL and Cr in tumor-bearing mice receiving PBS, 0.06 mg/kg Ber, 3 mg/kg EV-ctrl, 5 mg/kg High Ber or 3 mg/kg EV-ber treatments for 12 days ($n = 6$). The survival observation and growth observation were two independent experiments. Mean ± SEM and P values are shown. ns, not significant.

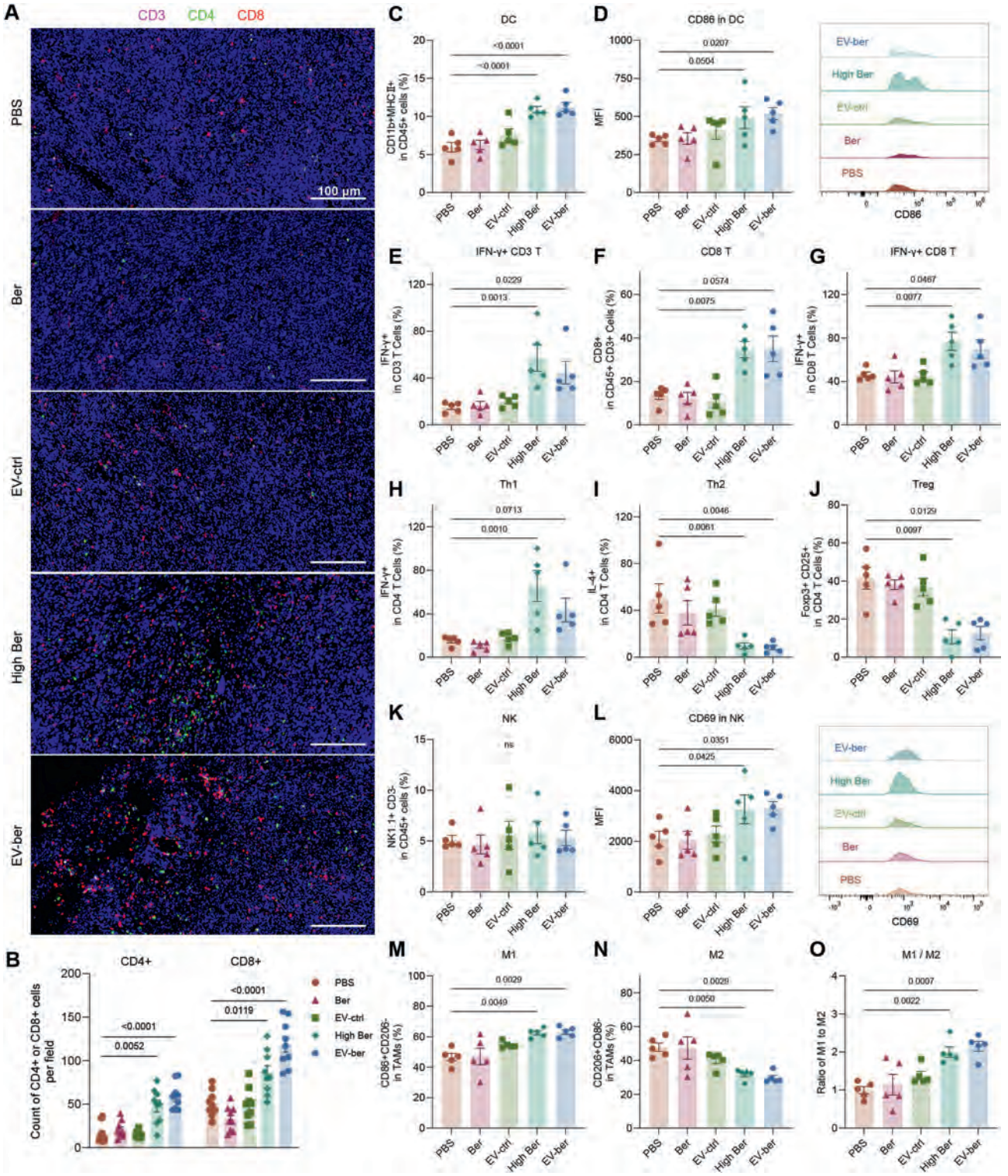

Figure 6 EV-ber reshapes tumor immune microenvironment and activates adaptive immune responses. Mice with LLC-subcutaneous tumors were treated with PBS, 0.06 mg/kg Ber, 3 mg/kg EV-ctrl, 5 mg/kg High Ber or 3 mg/kg EV-ber for 12 days, and then tumors were collected for measuring immune cells in TIME by IHC or flow cytometry. (A) The representative fluorescence images of $CD3^+$, $CD4^+$ and $CD8^+$ cells in the tumor tissues. (B) The counts of $CD4^+$ and $CD8^+$ cells per field of tumor tissues. $n = 9$ fields for 3 mice, ANOVA and Tukey test. (C−O) Multicolor flow cytometry revealing the proportions or ratios of DCs (C), CD86 MFI of DCs (D), IFNγ^+ T cells (E), $CD8^+$ T cells (F), IFN$\gamma^+$$CD8^+$ T cells (G), Th1 cells (H), Th2 cells (I), Tregs (J), NK cells (K), CD69 MFI of NK cells (L), M1-type TAMs (M), M2-type TAMs (N) and M1/M2 ratio (O) in tumors. $n = 5$, ANOVA and Tukey test. Mean ± SEM and P values are shown. ns, not significant. MFI, mean fluorescent intensity.

results showed that High Ber and EV-ber treatment significantly stimulated the infiltration ratio of DCs and mDCs, which are the initiators of anti-tumor immunity[50] (Fig. 6C and D). More importantly, although the overall proportion of T cells and $CD4^+$ T cells (Supporting Information Fig. S6A−S6C) did not change, the treatment with High Ber and EV-ber significantly increased the proportion of activated T cells, that is, IFN-γ^+ T cells (Fig. 6E), as well as the proportion of $CD8^+$ T cells and IFNγ^+CD8^+ T cells (Fig. 6F and G). In addition, the proportion of Th1 cells, which are considered beneficial for anti-tumor immunity, significantly increased after treatments (Fig. 6H), while the proportion of Th2 cells and Treg cells, which are considered unfavorable for anti-tumor immunity, significantly decreased (Fig. 6I and J, Fig. S6D). As a subset of whole innate lymphoid cells, NK cells are currently defined as effector cells similar to cytotoxic T cells (CTLs), exerting natural cytotoxicity against primary tumor cells and metastasis by inhibiting proliferation, migration and colonization to distant tissues[35]. The results showed the overall proportion of NK cells and NKT cells did not change (Fig. 6K, Fig. S6E), but the mean fluorescence intensity of CD69 in NK cells, significantly increased after treatments, indicating the activated NK cells increasing (Fig. 6L). The changes in myeloid cells were mainly reflected in a significant increase in the proportion of M1-type TAMs (Fig. 6M), a significant decrease in M2-type TAMs (Fig. 6N), and a significant increase of the M1/M2 ratio (Fig. 6O), while the proportions of TAMs, granu-myeloid-derived suppressor cells (G-MDSCs), and mono-myeloid-derived suppressor cells (M-MDSCs) did not change significantly (Fig. S6F and S6H). As we know, tumor-promoting inflammation disturbs normal myelopoiesis, which generates immunosuppressive myeloid cells such as MDSCs that could suppress effector lymphocytes[33]. TAMs belong to immunosuppressive myeloid cells[33], with complex roles in TIME. For instance, M2-type TAMs support tumor growth by enhancing angiogenesis and suppressing T cells, while M1-type TAMs reject it by killing tumor cells through arginine metabolism[51]. Therefore, it can be said that a series of changes in myeloid cells after treatments indicate the formation of a favorable anti-tumor immune microenvironment.

Together, our results reveal that both sole berberine and EV-ber treatments could induce an improved TIME that is benefit to inhibit LUAD progression, thereby explaining the encouraging effects of sole berberine and EV-ber on tumor-bearing mice.

3.7. EV-ber modulates intratumoral microbial-immune network in LUAD

At the beginning of this study, we have proved that a certain number of microbes exist in human LUAD tissues and unevenly distribute in various cell populations within the tumor, and this existence has been defined as the intratumoral microbiome[3,52]; moreover, we have also proved that berberine has a heterogeneous effect on different bacteria, and that free berberine and berberine-loaded EV-ber can resist LUAD *in vivo* and *in vitro* and reshape the TIME. Therefore, in this section, we aimed to investigate whether berberine and EV-ber could influence the intratumoral microbiome in mouse LUAD and its potential association with the TIME. First, we performed absolute quantitative qPCR to measure the total bacterial load in tumor tissues from tumor-bearing mice treated with different regimens. The mean bacterial count in the High Ber and EV-ber groups was reduced by nearly half a million compared to that in the PBS or EV-ctrl groups (Fig. 7A). Subsequently, we conducted immunohistochemical staining of lipopolysaccharide (LPS, a specific component of Gram-negative bacteria) and lipoteichoic acid (LTA, a characteristic component of Gram-positive bacteria) in tumor tissues to visualize changes in the intratumoral microbiome (Fig. 7B). Both the mean positive area (Fig. 7C) and average optical density value (Supporting Information Fig. S7A), quantified using ImageJ software, were significantly lower in the High Ber and EV-ber groups compared to the control groups. After normalizing the positive area data of each group relative to the PBS group, no statistically significant difference was found in the degree of inhibition between LPS and LTA ($P = 0.7176$, for all groups) (Fig. 7D). Together, our results revealed that both free berberine and EV-ber could reduce the total amount of intratumoral bacteria without discrimination between the Gram+ or Gram− bacteria. The decrease of intratumoral microbiome amount, or said as bacteria death, could possibly activate antitumor immunity[53,54], partly explaining why EV-ber treatment could improve TIME.

To further investigate the specific changes in the intratumoral microbiome, we conducted a microbiome sequencing. Due to the low mass of bacteria in tumor sites, library construction for 16S rDNA sequencing failed, but we achieved successful library construction for 2bRAD-M gene sequencing, which has higher sensitivity and accuracy. In terms of alpha diversity, the High Ber and EV-ber groups had more abundant microbial communities than the controls (Chao, Wilcoxon test, $P = 0.0959$) (Fig. 7E, left). Beta diversity analysis using non-metric multidimensional scaling (NMDS) revealed clear differences in microbial composition between the four groups based on Bray-Curtis distance (stress = 0.173) (Fig. 7E, right). LEfSE analysis identified 14 discriminative features (LDA score$\geq$2.0) with significantly different relative abundance among the four groups (Fig. 7F). At both the genus and species level, the microbial compositions of the four groups were distinct from each other (Fig. S7B and S7C). At the well-studied phylum level, we observed that several taxa leading to tumorigenesis, including *Fusobacteria*[55−57], *Tenericutes*[58] and *Basidiomycota*[59], decreased in EV-ber treated tumors, while the taxa regarded as probiotics protecting from cancers, such as *Bacteroidetes*[60], increased in EV-ber treated tumors (Fig. 7G). Together, different treatments, including EV-ctrl, resulted in different compositions of the intratumoral microbiome; EV-ber treatment could increase the "beneficial" microbes and decreased the "harmful" ones.

Subsequently, we established a subcutaneous tumor model with intratumoral bacterial clearance (ABTx) to elucidate the therapeutic mechanisms of berberine and EV-ber. Notably, the removal of intratumoral bacteria did not alter tumor progression ($P = 0.9015$), but significantly attenuated the therapeutic effects of both High Ber and EV-ber ($P = 0.0844$ and 0.0511, respectively). Importantly, the therapeutic effects of High Ber and EV-ber in ABTx model mice remained significantly higher compared to untreated ABTx mice (both $P < 0.0001$; Fig. 7H). The ABTx model had no impact on mouse body weight, and the observed weight loss in the berberine-treated groups was consistent with previous findings (Fig. 7I). These results suggest that the therapeutic mechanisms of berberine and EV-ber involve both modulation of the intratumoral microbiota and direct antitumor effects.

Subsequently, we investigated whether the intratumoral microbiome alterations induced by EV-ber could influence TIME, aiming to explain how berberine and EV-ber reshape the TIME. To identify the specific microbial and immunological targets associated with berberine's effects in combination with intratumoral microbes and antitumor immunity, we systematically

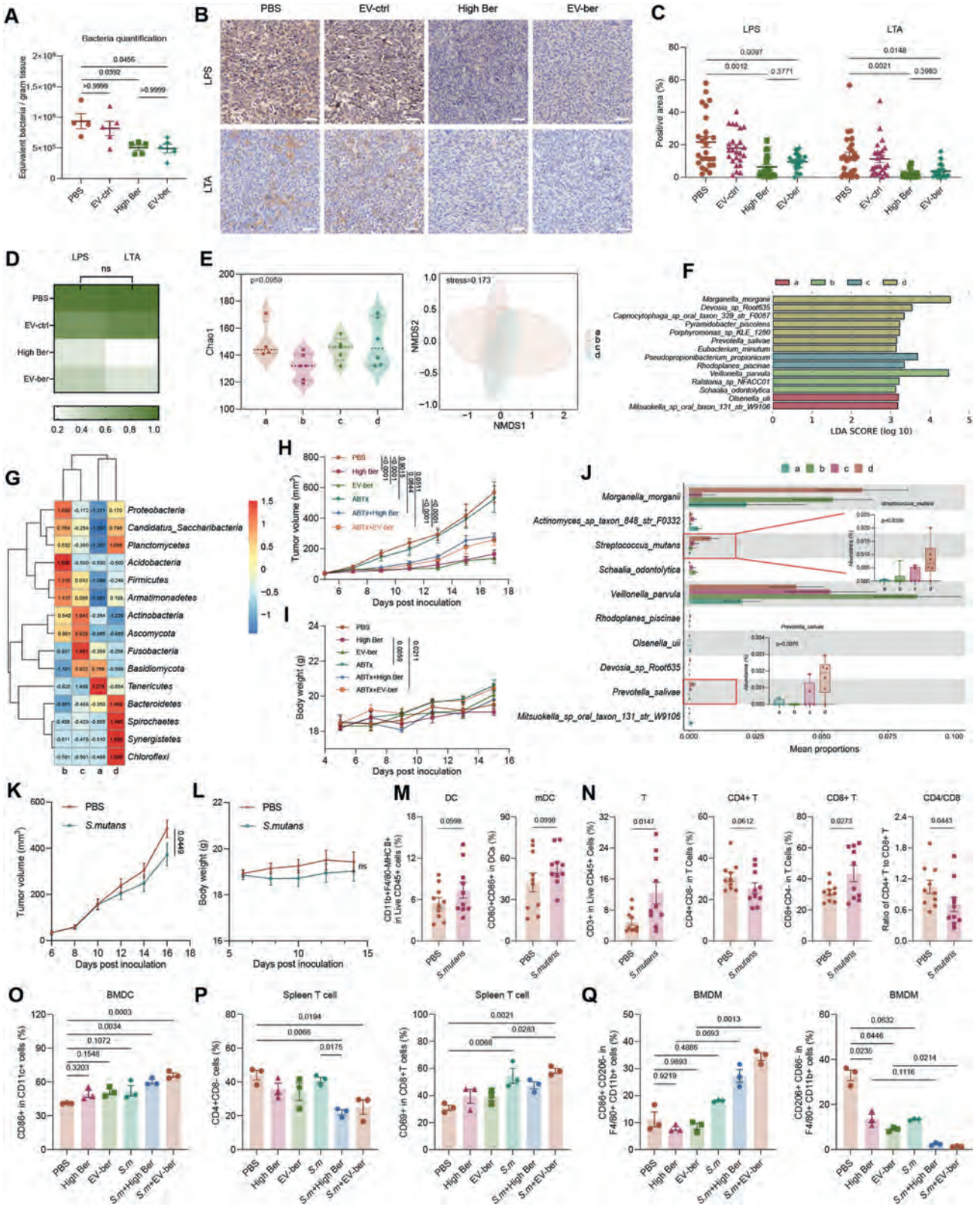

Figure 7 EV-ber modulates intratumoral microbial-immune network in LUAD. (A) The absolute quantitative qPCR for V9 region indicating the amount of bacteria in LLC-subcutaneous tumors from the mice treated with PBS, 3 mg/kg EV-ctrl, 5 mg/kg High Ber or 3 mg/kg EV-ber for 12 days ($n = 4$ or 5). Kruskal-Wallis test. IHC staining LPS and LTA manifesting the content of intratumoral Gram- and Gram+ bacteria in LLC-subcutaneous tumors from the mice treated with PBS, 3 mg/kg EV-ctrl, 5 mg/kg High Ber or 3 mg/kg EV-ber for 12 days. (B) The representative images of IHC staining LPS and LTA for different groups. Scale bars: 40 μm. (C) The results of positive area of LPS and LTA, (D) and the normalized positive area of LPS and LTA manifested by heatmap. $n = 25$ fields for 5 samples. ANOVA and Tukey test. (E) (left) The alpha

analyzed the 2bRAM-D sequencing data. During multiple-group significance analysis using one-way ANOVA, we found that the abundances of *Prevotella salivae* and *Streptococcus mutans* were significantly higher in the High Ber and EV-ber groups compared to the PBS and EV-ctrl groups (Fig. 7J). The Kruskal-Wallis test further confirmed that the abundances of *Capnocytophaga* sp. *oral taxon 329 str. F0087*, *Porphyromonas* sp. *KLE_1280*, and *Prevotella salivae* were significantly elevated in the High Ber and EV-ber groups relative to the controls (Fig. S7D). The consistent changes in these bacterial taxa between the EV-ber and High Ber groups suggest that these effects are primarily attributable to berberine itself, rather than other confounding factors. Among the three differentially abundant taxa, *Streptococcus mutans* (*S. mutans*) exhibited the highest abundance (over 0.5%), indicating its potential biological relevance. Recent studies have shown that the introduction of *S. mutans* into therapeutic biomaterials can promote DC maturation and T cell activation within the TIME[61]. We hypothesized that increased *S. mutans* within tumors could modulate immune infiltration. To eliminate the influence of confounding factors, 5×10^6 *S. mutans* were directly injected into LLC subcutaneous tumors. Surprisingly, mice receiving *S. mutans* injections exhibited significantly smaller tumors than the control group after 10 days of observation ($P = 0.0449$; Fig. 7K), with no observable impact on body weight (Fig. 7L). Subsequently, we collected tumor tissues and performed multicolor flow cytometry analysis. In contrast to the previous experiment (Fig. 6), the observed immune changes were primarily associated with adaptive immunity, including increased levels of DCs and mature DCs (Fig. 7M), as well as a significant increase in total T cells and $CD8^+$ T cells, accompanied by a decrease in $CD4^+$ T cells and a reduced CD4/CD8 ratio (Fig. 7N). However, no significant changes were observed in innate immune cell populations, including tumor-associated macrophages (TAMs), M1-type TAMs, M2-type TAMs, or NK cells (Fig. S7E). Furthermore, we validated these findings using primary immune cells. The presence of *S. mutans* enabled both High Ber and EV-ber to significantly enhance CD86 expression in bone marrow-derived dendritic cells (BMDCs) (Fig. 7O). It also led to a reduction in $CD4^+$ T cells and an increase in $CD69^+CD8^+$ T cells in primary T cell cultures (Fig. 7P), although no significant effect was observed on total $CD8^+$ T cells (Fig. S7F). Additionally, *S. mutans* significantly enhanced the ability of berberine and EV-ber to promote the differentiation of bone marrow-derived macrophages (BMDMs) toward the M1 phenotype while inhibiting their differentiation into the M2 phenotype (Fig. 7Q). Notably, *S. mutans* alone did not induce significant changes, which was consistent with the *in vivo* results.

In conclusion, our data indicated that EV-ber could reduce the bacterial content within the tumor, alter its composition, and influence the specific anti-tumor immunity by changing the intratumoral microbiome. This proved that the intratumoral microbiome was an intermediate link from EV-ber to the TIME, consistent with our previous hypothesis.

3.8. EV-ber inhibits metastasis and enhances the anti-LUAD activity of anti-PD-L1 antibody

Our above results demonstrated that subcutaneous tumors in mice harbored a certain quantity of bacteria, which could be significantly reduced by EV-ber treatment. A recent study indicated that tumor-resident intracellular microbiota (particularly viable bacteria) could promote metastatic colonization in breast cancer[5]. Based on this study, we designed a modified experimental protocol to evaluate the anti-metastasis effect of EV-ber treatment through the reduction of the intratumoral microbiome (Fig. 8A). Briefly, we established LLC-GFP subcutaneous tumors in mice over a 20-day period to allow the formation of an intratumoral microbiome. Subsequently, the tumors were dissociated, and LLC-GFP cells-excluding other cell types-were isolated using fluorescence-activated cell sorting (FACS). Finally, these purified cells were injected into the tail vein of a new cohort of mice to establish a metastasis model. Aikun Fu et al.'s[5] results showed nearly 80% of tumor-resident microbes resided in the cytosol, which supported us using tumor cells to build up metastasis model. Over nearly three weeks to allow metastasis to develop, we observed significantly fewer metastatic foci throughout the body in mice that received High Ber or EV-ber-treated LLC-GFP cells (Fig. 8B), and these groups also exhibited significantly longer overall survival (Fig. 8C). Since the lungs are the primary site of systemic metastasis, we dissected the entire lungs from each mouse and prepared whole-lung paraffin-embedded sections. Consistent with the whole-body findings, HE staining of the whole-lung paraffin sections revealed a reduction of over 30% in the metastatic burden in mice derived from High Ber or EV-ber-treated LLC-GFP cells compared to the controls (Fig. 8D). Collectively, these results demonstrate that both free berberine and EV-ber are capable of inhibiting tumor metastasis.

The tumor microenvironment is a complex system where malignant cells interact with immune and non-immune cells individually or in combination to affect sensitivity to immunotherapy[62,63]. Given the remodeling of the tumor immune microenvironment induced by High Ber and EV-ber, characterized by the enrichment of mDCs and $CD8^+$ T cells, we sought to investigate whether free berberine and EV-ber could enhance the therapeutic efficacy of anti-PD-L1 (αPD-L1) treatment by evaluating tumor growth. The treatment schedules for LLC tumor-bearing mice are summarized in Fig. 8E. Notably, no significant

diversity (Chao, Wilcoxon test), (right) and Beta diversity (NMDS) of four groups. (F) LEfSE analysis uncovering discriminative features with significant different relative abundance between four groups at species level. (G) Heatmap showing the relative abundance of top 30 taxa in the four groups at phylum level. The G-score values are shown. The tumor volume (H) and body weight (I) of the mice with LLC-subcutaneous tumors treated with PBS, 5 mg/kg High Ber, 3 mg/kg EV-ber, ABTx, ABTx plus High Ber, or ABTx plus EV-ber for 12 days ($n = 6$). ANOVA and Tukey test. (J) Barplot showing the significant differential relative abundance of the taxa in four groups, and significantly increased *S. mutans* and *P. salivae* in High Ber and EV-ber groups. ANOVA. Groups: a, PBS, b, EV-ctrl, c, High Ber, d, EV-ber, $n = 4-6$. The tumor volume (K) and body weight (L) of the mice with LLC-subcutaneous tumors treated by PBS or 5×10^6 *S. mutans*. ANOVA and Tukey test. (M, N) Multicolor flow cytometry revealing the proportions or ratios of tumor infiltrating (M) DCs and mDCs, and (N) T cells, $CD4^+$ T cells, $CD8^+$ T cells and CD4/CD8 ratio of PBS or *S. mutans* treated mice ($n = 10$). Student's *t* test. (O−Q) The changes in cell differentiation of BMDCs (O), spleen T cells (P), and BMDMs (Q) treated with PBS, 38.983 μg/mL berberine (High Ber), 60 μg/mL EV-ber, *S. mutans* (MOI 20:1), *S. mutans* plus High Ber, and *S. mutans* plus EV-ber, respectively, for 18 h ($n = 3$). ANOVA and Tukey test. Mean ± SEM and *P* values are shown. ns, not significant.

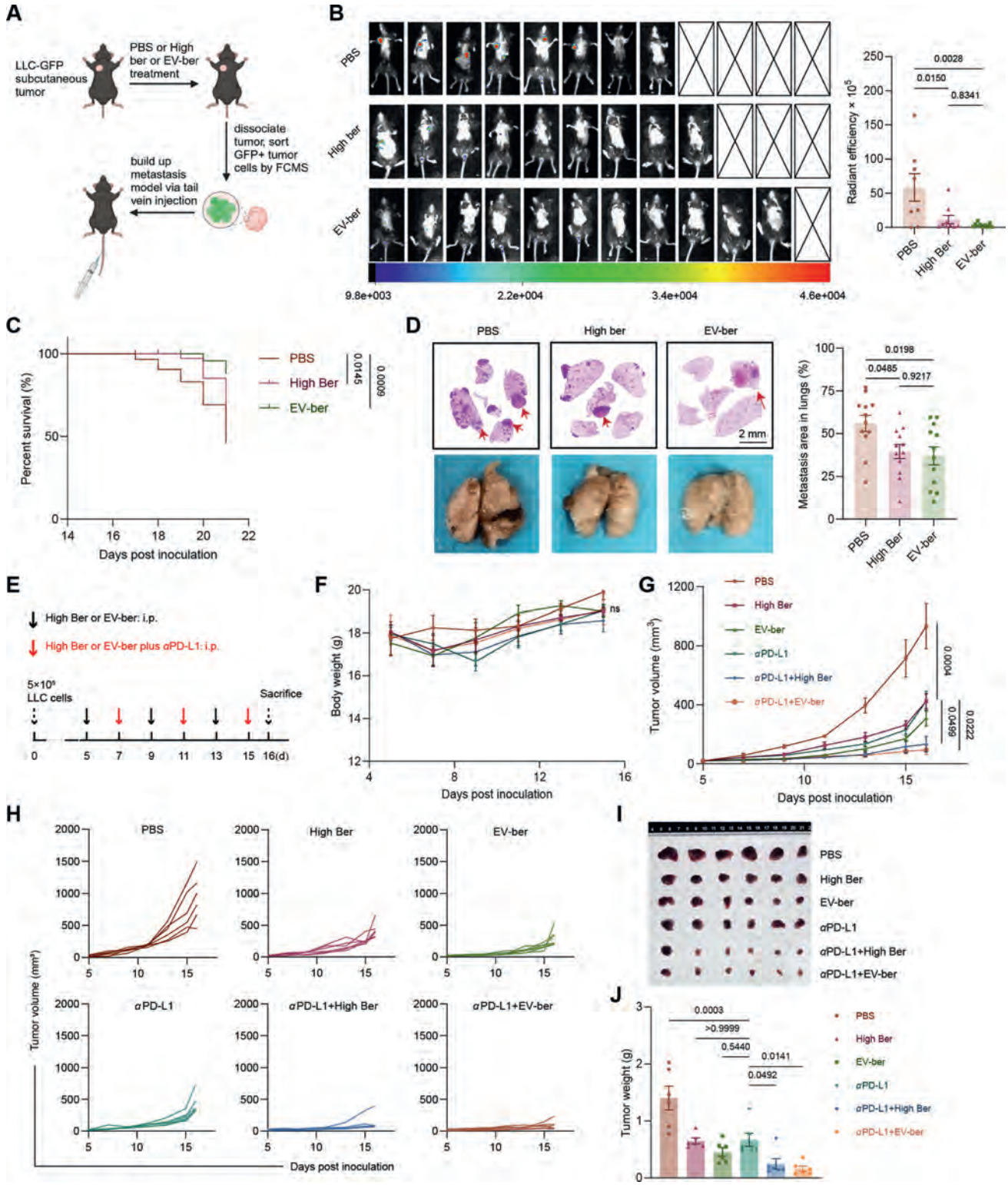

Figure 8 EV-ber inhibits metastasis and enhances the anti-LUAD activity of anti-PD-L1 antibody. (A) Illustration for metastasis experimental process. (B) The images of mice taken by IVIS for observing metastasis foci throughout body, and the blank boxes with check manifesting mice died before taking IVIS. The radiant efficiency of IVIS images showed. $n = 7-11$, ANOVA and Tukey test. (C) The Kaplan−Meier curves of metastatic mice survival rates after about 3 weeks for metastasis formation. $n = 12$, Mantel−Cox test. (D) The representative images of HE staining for paraffin sections embedded with whole lungs and corresponding photos, and the results of metastasis area in lungs. $n = 11$, ANOVA and Tukey test. (E) Illustration for combination therapy experimental process. Both the single dose of High Ber and αPDL1 was 5 mg/kg. The mean body weight (F) and mean tumor volume (G) of tumor-bearing mice receiving the treatments of PBS, High Ber, EV-ber, αPD-L1, αPD-L1 plus High Ber and αPD-L1 plus EV-ber for 12 days. $n = 6$, ANOVA and Tukey test. (H) The tumor growth curves of tumor-bearing mice, (I) the

decrease in body weight was observed in any of the treatment groups (Fig. 8F). Tumor growth curves and representative images of excised tumors are presented in Fig. 8G−I. The mean tumor weight data showed that αPD-L1 treatment alone resulted in nearly a 50% reduction in tumor growth. Importantly, combining αPD-L1 with either High Ber or EV-ber further enhanced the therapeutic effect compared to αPD-L1, High Ber, or EV-ber monotherapy (Fig. 8J). Collectively, these findings highlight the potential and safety of EV-ber as a complementary strategy to improve the efficacy of αPD-L1 treatment, underscoring its broad therapeutic value.

4. Discussion

Emerging evidence suggests that bacteria within the tumour-associated microbiota play pivotal roles in cancer development[64], metastasis[5−7], immunosurveillance[8,65,66] and chemoresistance[9,10]. In this study, we demonstrated that intratumoral bacteria, as a fundamental component of the TME in lung cancer, exhibit distinct cellular distribution patterns. By integrating host-bacterial immune−cell interaction mapping within the TME using scRNA-seq data, we identified several targeting bacterial genera—*Lysinibacillus*, *Stenotrophomonas*, *Weissella*, *Comamonas*, and *Aeromonas*—among the significantly differentially abundant bacteria between LUAD and normal tissues. These bacterial genera were categorized as either beneficial or harmful based on their associations with various immune cell populations. Following *in vivo* validation of their respective anti- or pro-tumor roles, we identified berberine as a promising candidate drug capable of re-educating the microbial community by selectively reducing harmful microbes while preserving beneficial ones. Encapsulation of berberine into tumor cell-derived EVs enhanced its tumor-targeting capability for *in vivo* applications. EV-ber effectively re-educated the intratumoral microbiome and modulated multiple immunological processes. *In vivo* administration of EV-ber inhibited subcutaneous tumor growth, synergized with anti-PD-L1 immunotherapy, and reduced metastatic potential in mouse models. To the best of our knowledge, this study is the first to confirm, based on single-cell RNA-seq data analysis, that specific intratumoral bacteria represent actionable anticancer targets for future innovative cancer therapies. Re-education of tumor-associated microbiome thus represents a feasible and promising strategy for tumor therapy.

Microbiome composition can significantly vary between individuals[3,52,67], posing challenges in translating bacterial characteristics identified in large-scale population studies to individual patients. The heterogeneity of microbial communities presents a major challenge in translating findings from large-scale population datasets into effective personalized treatments. As a result, bacterial therapies derived from population-level data may exhibit limited response rates across individual patients. To overcome this limitation, we propose the concept of tailoring intratumoral microbiota specifically derived from individual cancer patients, which could offer unique anticancer efficacy and represent a novel form of personalized medicine. In our study, we employed scRNA-seq to identify bacterial populations within the tumor microenvironment that may serve as effective anticancer targets for lung cancer therapy. First, we screened for bacteria that were differentially distributed between tumor and adjacent normal tissues to identify potentially relevant microorganisms. We then subtyped these intratumoral bacteria based on their associations with specific immune cell populations, as well as their correlations with cell-type-specific gene expression profiles and molecular pathways. This in-depth analysis enabled us to identify bacterial taxa with potential immunomodulatory functions within the tumor microenvironment. Although the precise mechanisms by which intratumoral microorganisms influence immune cells remain to be fully elucidated, classifying bacterial populations according to their spatial and functional relationships with immune cells provides valuable mechanistic insights. Our findings were further validated through *in vivo* experiments, confirming the associations between specific bacterial communities and immune cell activities. This comprehensive "find-and-subtype" strategy not only identifies key intratumoral microbiota but also adapts the analysis to the unique biological characteristics of each lung cancer patient. By leveraging the distinct microbiome profiles of individual patients, this personalized approach holds promise for the development of targeted microbial therapies that move beyond generic, one-size-fits-all interventions.

Targeting tumor-associated microorganisms has garnered increasing attention, with most studies focusing primarily on either eliminating harmful microbes or supplementing beneficial ones as standalone therapeutic strategies. The development of nanomaterials-based approaches for modulating intratumoral microbiota offers promising potential for cancer treatment. For example, a dual-cascade responsive nanoparticle system has been developed and shown to significantly enhance the therapeutic efficacy against pancreatic cancer by specifically eliminating tumor-resident intracellular bacteria[26]. Gallium-polyphenol network functionalized by probiotics was able to modulate the intratumor microbiota and promote anti-tumor immune responses in pancreatic cancer[68]. In addition, liposomal antibiotic formulations have been formulated to eliminate tumor-associated bacteria, ultimately resulting in the release of neoantigens and eliciting antitumor immune responses[69]. However, our study employs a more comprehensive strategy by simultaneously screening for both beneficial and harmful microbial populations within the tumor microenvironment. By identifying compounds that exhibit potent antimicrobial activity against harmful bacteria while preserving the growth of beneficial species, we aim to achieve a dual therapeutic outcome—effectively eliminating detrimental microorganisms while promoting the enrichment of advantageous microbes. This approach, which seeks to redirect the intratumoral microbiota toward an anti-tumor phenotype rather than completely eradicating microbial communities, theoretically offers a more robust strategy compared to methods that focus solely on supplementing or depleting specific microbial groups. In this study, we evaluated the feasibility of this strategy using 2bRAM-D sequencing technology, which allowed us to analyze and characterize the composition of the intratumoral microbiome. Our findings revealed that EV-ber exerted a significant modulatory effect on the intratumoral microbial community. A comparison of the differentially abundant microbial taxa between the PBS-treated and EV-ber-treated groups, supported by both literature evidence and subsequent intratumoral injection experiments, confirmed the

appearance of tumors, (J) and the mean weight of naked tumors, ANOVA and Tukey test. Mean ± SEM and *P* values are shown. ns, not significant.

establishment of a restructured microbial community. This newly formed microbiota displays an anti-tumor phenotype, suggesting that EV-ber may facilitate a beneficial "re-education" of the intratumoral microbiome. Reprogramming the intratumoral microbiome to support anti-tumor immune responses represents a promising and innovative strategy for cancer therapy. By reshaping the microbial ecosystem within the tumor microenvironment—rather than simply aiming for broad elimination or supplementation—this approach may open new avenues for the development of more effective cancer treatments.

Regarding the synthesis of EV-ber, we introduced modifications to our existing preparation protocol. These modifications were necessary due to the poor aqueous solubility of berberine, which presents a major challenge for efficient encapsulation into EVs using conventional co-incubation methods. After a comprehensive evaluation of various encapsulation techniques, electroporation was selected as the optimal method, demonstrating superior loading efficiency. Subsequent *in vitro* and *in vivo* experiments revealed that EV-ber exhibited significantly improved tumor-targeting capability, enhanced anti-tumor efficacy, and a more favorable safety profile—even when compared to free berberine administered at a 40-fold higher dose. These results highlight the capacity of EV-ber to substantially improve the bioavailability of berberine, supporting its potential as a promising therapeutic platform for a range of berberine-associated diseases.

We further characterized the complex immune landscape modulated by EV-ber in lung carcinoma-bearing mice using multicolor flow cytometry. Enhanced dendritic cell maturation, increased infiltration of $CD8^+$ T cells, polarization toward M1-type tumor-associated macrophages, and activation of NK cells were observed. These findings indicate that EV-ber reshapes the TIME into a phenotype that is conducive to effective tumor suppression. Notably, a similar pattern of immune modulation was detected in mice treated with high-dose free berberine, confirming that EVs serve as efficient delivery vehicles that enhance the therapeutic performance of berberine. As anticipated, both free berberine and EV-ber led to a reduction in overall intratumoral microbial populations. Previous studies have demonstrated that intratumoral microbiota can accelerate drug degradation, thereby compromising therapeutic efficacy[26,43]. This suggests that the observed reduction in intratumoral microbiota may prolong the residence time of berberine at the tumor site, thereby ensuring sustained therapeutic efficacy. To further explore the relationship between intratumoral microbiota and immune modulation, we administered *Streptococcus mutans*—a bacterial species significantly enriched during berberine treatment—as a representative model. Remarkably, this intervention recapitulated the immune infiltration changes observed with both EV-ber and free berberine, including a reshaped TIME marked by enhanced immune activation. These findings underscore the pivotal yet complex role of the intratumoral microbiome in shaping the tumor immune response and suggest that the immunomodulatory effects of microbiota may partially contribute to the anti-tumor activity of EV-ber. Our study highlights the significant impact of EV-ber on modulating both the TIME and the intratumoral microbiome. Nevertheless, further research is needed to elucidate the precise molecular mechanisms involved.

As shown in Fig. S7G, the abundance of *Lysinibacillus*, *Stenotrophomonas*, *Weissella*, *Comamonas*, and *Aeromonas* in subcutaneous LLC tumors was markedly different from that observed in human LUAD tissues. We acknowledge that preclinical efficacy may not directly translate to clinical settings due to fundamental species differences and interpatient heterogeneity. When translating findings from murine models to patients with similar intratumoral microbiome profiles, key biological discrepancies must be carefully considered, including differences in microbiome composition and colonization patterns[70–72], immune disparities, and environmental exposures. Human microbiota transplants in gnotobiotic mice often fail to replicate donor profiles due to colonization barriers, anaerobic species loss, and underrepresentation of mucosa-adherent bacteria[70,71]. To overcome these limitations, we propose the use of non-human primate models and human lung organoid-microbiota co-cultures, combined with strategies to simulate clinical heterogeneity through patient-specific microbiota profiling and stratified analyses. For broader clinical application, we address interpatient variability—confirmed in single-cell datasets—by implementing biomarker-guided stratification (*e.g.*, our five-bacterial signature), personalized interventions, and adaptive trial designs targeting eligible subgroups. While tailoring therapy based on microbiome composition, we also explore the broader applicability of EV-ber. Future studies will determine whether its therapeutic efficacy is dependent on specific microbiome regulation or extends to more general microbial communities and conserved biological pathways—findings that are critical for its universal clinical translation.

5. Conclusions

We have developed an innovative strategy to identify and subtype the microbiome in lung cancer patients through the analysis of human single-cell datasets. By conducting a comprehensive screening of a compound library, berberine was identified as a promising candidate capable of not only eliminating harmful bacteria but also promoting the proliferation of beneficial microbial species. Our findings further demonstrate that berberine exhibits significant anti-LUAD activity both *in vitro* and *in vivo*. Building on these observations, we successfully synthesized berberine-loaded extracellular vesicles (EV-ber), which significantly enhanced the anti-LUAD efficacy of berberine in LLC tumor-bearing C57BL/6 mice. Notably, EV-ber also displayed a pronounced anti-metastatic effect and synergized effectively with anti-PD-L1 immunotherapy in the treatment of LUAD. At the mechanistic level, we confirmed that EV-ber modulates the immune-microbial network within the tumor microenvironment, shifting it toward an anti-tumor phenotype. Our research highlights a novel strategy for identifying key intratumoral microbiota and provides a personalized therapeutic approach tailored to individual lung cancer patients. We demonstrate that reprogramming the intratumoral microbiome toward an anti-tumor state—rather than aiming for complete eradication—can effectively suppress tumor growth. We anticipate that this innovative therapeutic strategy will hold broad applicability in the treatment of tumors where the presence of intratumoral microbiome has been pathologically confirmed.

Ethic statement

Our study was carried out according to the Declaration of Helsinki. The animal study was approved by Animal Care and Use Committee of Tongji Medical College, Huazhong University of Science and Technology [(2022) IACUC (3352)].

Acknowledgements

We thank Wenjing Xiong and Shanghai Universal Biotech Co., Ltd. for their help with instructing flowcytometry analysis. We thank Qingdao OE Biotech Co., Ltd. for their help with conducting 2bRAM-D. We thank Wuhan ProNets Biotechnology Co., Ltd. for their help with conducting HPLC. We are grateful for all the staff in the Center for Translational Medicine and Central Lab in Wuhan Union Hospital for their daily help. We also thank Animal Center of Huazhong University of Science and Technology for supporting the animal care service. This work was supported by National Science and Technology Major Project of the Ministry of Science and Technology of China (2022YFF1203300), National Natural Science Foundation of China (Nos. 82330003, 82100112, 82200112), Hubei Province Key Research and Development Project (2022BCA016, 2023BCB146, China), Hubei Provincial Natural Science Foundation of China (2023AFB1073), Hubei Provincial Department of Science and Technology (2024DJA023, China), and Hubei Key Laboratory of Biological Targeted Therapy (2023swbx005, China).

Author contributions

Jingjing Deng, Mengfei Guo and Yang Jin designed the study; Jingjing Deng, Wenlong Kuang, Wenjuan Chen, E Zhou, and Yali Wu participated the experiments; Zimo Yang, Jiangbin Chen, Xinghui Cao, Zhengrong Yin, Jiatong Liu, Minglei Li, Feng Wu, and Jinshuo Fan provided drugs or suggestions for designing and writing; Mengfei Guo and Yang Jin reviewed the final manuscript. All of the authors have read and approved the final manuscript.

Conflicts of interest

The authors have no conflicts of interest to declare.

Appendix A. Supporting information

Supporting Information to this article can be found online at https://doi.org/10.1016/j.apsb.2025.12.014.

References

1. Miller M, Hanna N. Advances in systemic therapy for non-small cell lung cancer. *BMJ* 2021;**375**:n2363.
2. Deng J, Zhou M, Liao T, Kuang W, Xia H, Yin Z, et al. Targeting cancer cell ferroptosis to reverse immune checkpoint inhibitor therapy resistance. *Front Cell Dev Biol* 2022;**10**:818453.
3. Nejman D, Livyatan I, Fuks G, Gavert N, Zwang Y, Geller LT, et al. The human tumor microbiome is composed of tumor type-specific intracellular bacteria. *Science* 2020;**368**:973−80.
4. Dohlman AB, Klug J, Mesko M, Gao IH, Lipkin SM, Shen X, et al. A pan-cancer mycobiome analysis reveals fungal involvement in gastrointestinal and lung tumors. *Cell* 2022;**185**:3807−22.e12.
5. Fu A, Yao B, Dong T, Chen Y, Yao J, Liu Y, et al. Tumor-resident intracellular microbiota promotes metastatic colonization in breast cancer. *Cell* 2022;**185**:1356−72.e26.
6. Yang K, Hou Y, Zhang Y, Liang H, Sharma A, Zheng W, et al. Suppression of local type I interferon by gut microbiota-derived butyrate impairs antitumor effects of ionizing radiation. *J Exp Med* 2021;**218**: e20201915.
7. Bullman S, Pedamallu CS, Sicinska E, Clancy TE, Zhang X, Cai D, et al. Analysis of Fusobacterium persistence and antibiotic response in colorectal cancer. *Science* 2017;**358**:1443−8.
8. Pinato DJ, Howlett S, Ottaviani D, Urus H, Patel A, Mineo T, et al. Association of prior antibiotic treatment with survival and response to immune checkpoint inhibitor therapy in patients with cancer. *JAMA Oncol* 2019;**5**:1774−8.
9. Huang X-Z, Gao P, Song Y-X, Xu Y, Sun J-X, Chen X-W, et al. Antibiotic use and the efficacy of immune checkpoint inhibitors in cancer patients: a pooled analysis of 2740 cancer patients. *OncoImmunology* 2019;**8**:e1665973.
10. Shi Y, Zheng W, Yang K, Harris KG, Ni K, Xue L, et al. Intratumoral accumulation of gut microbiota facilitates CD47-based immunotherapy *via* STING signaling. *J Exp Med* 2020;**217**:e20192282.
11. Riquelme E, Zhang Y, Zhang L, Montiel M, Zoltan M, Dong W, et al. Tumor microbiome diversity and composition influence pancreatic cancer outcomes. *Cell* 2019;**178**:795−806.e12.
12. Wieland A, Patel MR, Cardenas MA, Eberhardt CS, Hudson WH, Obeng RC, et al. Defining HPV-specific B cell responses in patients with head and neck cancer. *Nature* 2021;**597**:274−8.
13. He D, Wang D, Lu P, Yang N, Xue Z, Zhu X, et al. Single-cell RNA sequencing reveals heterogeneous tumor and immune cell populations in early-stage lung adenocarcinomas harboring EGFR mutations. *Oncogene* 2021;**40**:355−68.
14. Wang C, Yu Q, Song T, Wang Z, Song L, Yang Y, et al. The heterogeneous immune landscape between lung adenocarcinoma and squamous carcinoma revealed by single-cell RNA sequencing. *Signal Transduct Targeted Ther* 2022;**7**:289.
15. Ghaddar B, Biswas A, Harris C, Omary MB, Carpizo DR, Blaser MJ, et al. Tumor microbiome links cellular programs and immunity in pancreatic cancer. *Cancer Cell* 2022;**40**:1240−53.e5.
16. Stuart T, Butler A, Hoffman P, Hafemeister C, Papalexi E, Mauck WM, et al. Comprehensive integration of single-cell data. *Cell* 2019;**177**:1888−902.e21.
17. Debnath A, Parsonage D, Andrade RM, He C, Cobo ER, Hirata K, et al. A high-throughput drug screen for Entamoeba histolytica identifies a new lead and target. *Nat Med* 2012;**18**:956−60.
18. Di Bonaventura G, Lupetti V, Di Giulio A, Muzzi M, Piccirilli A, Cariani L, et al. Repurposing high-throughput screening identifies unconventional drugs with antibacterial and antibiofilm activities against pseudomonas aeruginosa under experimental conditions relevant to cystic fibrosis. *Microbiol Spectr* 2023;**11**:e0035223.
19. Gu L, Zhang H, Liu T, Zhou S, Du Y, Xiong J, et al. Discovery of dual inhibitors of MDM2 and XIAP for cancer treatment. *Cancer Cell* 2016;**30**:623−36.
20. Guo M, Wu F, Hu G, Chen L, Xu J, Xu P, et al. Autologous tumor cell-derived microparticle-based targeted chemotherapy in lung cancer patients with malignant pleural effusion. *Sci Transl Med* 2019;**11**: eaat5690.
21. Chen W, Tan Q, Guo M, Liao T, Li Y, Yin Z, et al. Tumor cell-derived microparticles packaging monocarboxylate transporter4 inhibitor fluvastatin suppress lung adenocarcinoma *via* tumor microenvironment remodeling and improve chemotherapy. *Chem Eng J* 2023;**451**: eaat5690.
22. Wu Y, Chen W, Deng J, Cao X, Yang Z, Chen J, et al. Tumour-derived microparticles obtained through microwave irradiation induce immunogenic cell death in lung adenocarcinoma. *Nat Nanotechnol* 2025;**20**: 1119−30.
23. Wu Y, Chen W, Deng J, Zhou X, Chen J, Yang Z, et al. Cancer-associated fibroblast-derived extracellular vesicles loaded with GLUT1 inhibitor synergize anti-PD-L1 to suppress tumor growth *via* degrading matrix stiffness and remodeling tumor microenvironment. *J Control Release* 2025;**385**:113998.
24. Zhang G, Huang X, Xiu H, Sun Y, Chen J, Cheng G, et al. Extracellular vesicles: natural liver-accumulating drug delivery vehicles for the treatment of liver diseases. *J Extracell Vesicles* 2020;**10**:e12030.
25. Dong L, Zieren RC, Horie K, Kim CJ, Mallick E, Jing Y, et al. Comprehensive evaluation of methods for small extracellular vesicles

separation from human plasma, urine and cell culture medium. *J Extracell Vesicles* 2020;**10**:e12044.
26. Kang X, Bu F, Feng W, Liu F, Yang X, Li H, et al. Dual-cascade responsive nanoparticles enhance pancreatic cancer therapy by eliminating tumor-resident intracellular bacteria. *Adv Mater* 2022;**34**: e2206765.
27. Herfs M, Herman L, Hubert P, Minner F, Arafa M, Roncarati P, et al. High expression of PGE2 enzymatic pathways in cervical (pre) neoplastic lesions and functional consequences for antigen-presenting cells. *Cancer Immunol Immunother* 2009;**58**:603−14.
28. Ibekwe AM, Watt PM, Grieve CM, Sharma VK, Lyons SR. Multiplex fluorogenic real-time PCR for detection and quantification of *Escherichia coli* O157:H7 in dairy wastewater wetlands. *Appl Environ Microbiol* 2002;**68**:4853−62.
29. Wang S, Meyer E, McKay JK, Matz MV. 2b-RAD: a simple and flexible method for genome-wide genotyping. *Nat Methods* 2012;**9**: 808−10.
30. Hou Y, Zhang M, Jiang Q, Yang Y, Liu J, Yuan K, et al. Microbial signatures of neonatal bacterial meningitis from multiple body sites. *Front Cell Infect Microbiol* 2023;**13**:1169101.
31. Lesbats J, Brillac A, Reisz JA, Mukherjee P, Lhuissier C, Fernandez-Monreal M, et al. Macrophages recycle phagocytosed bacteria to fuel immunometabolic responses. *Nature* 2025;**640**:524−33.
32. Kang JH, Zappasodi R. Modulating Treg stability to improve cancer immunotherapy. *Trends Cancer* 2023;**9**:911−27.
33. Nakamura K, Smyth MJ. Myeloid immunosuppression and immune checkpoints in the tumor microenvironment. *Cell Mol Immunol* 2020; **17**:1−12.
34. Mellman I, Chen DS, Powles T, Turley SJ. The cancer-immunity cycle: indication, genotype, and immunotype. *Immunity* 2023;**56**: 2188−205.
35. Wu SY, Fu T, Jiang YZ, Shao ZM. Natural killer cells in cancer biology and therapy. *Mol Cancer* 2020;**19**:120.
36. Martin-Perez M, Urdiroz-Urricelqui U, Bigas C, Benitah SA. The role of lipids in cancer progression and metastasis. *Cell Metab* 2022;**34**: 1675−99.
37. Liu L, Du Y, Du Y, Yan W, Li Y, Cui K, et al. Exopolysaccharide from Weissella confusa J4-1 inhibits colorectal cancer *via* induction of cell cycle arrest. *Int J Biol Macromol* 2023;**253**:127625.
38. Zhao R, Coker OO, Wu J, Zhou Y, Zhao L, Nakatsu G, et al. Aspirin reduces colorectal tumor development in mice and gut microbes reduce its bioavailability and chemopreventive effects. *Gastroenterology* 2020;**159**:969−83.e4.
39. Rodríguez-García A, Arroyo A, García-Vicente R, Morales ML, Gómez-Gordo R, Justo P, et al. Short-chain fatty acid production by gut microbiota predicts treatment response in multiple myeloma. *Clin Cancer Res* 2024;**30**:904−17.
40. Liu B, Zhou Z, Jin Y, Lu J, Feng D, Peng R, et al. Hepatic stellate cell activation and senescence induced by intrahepatic microbiota disturbances drive progression of liver cirrhosis toward hepatocellular carcinoma. *J Immunother Cancer* 2022;**10**:e003069.
41. Diot C, García-González AP, Vieira AF, Walker M, Honeywell M, Doyle H, et al. Bacterial diet modulates tamoxifen-induced death *via* host fatty acid metabolism. *Nat Commun* 2022;**13**:5595.
42. Di Chiacchio IM, Gómez-Abenza E, Paiva IM, de Abreu DJM, Rodríguez-Vidal JF, Carvalho EEN, et al. Bee pollen in zebrafish diet affects intestinal microbiota composition and skin cutaneous melanoma development. *Sci Rep* 2022;**12**:9998.
43. Geller LT, Barzily-Rokni M, Danino T, Jonas OH, Shental N, Nejman D, et al. Potential role of intratumor bacteria in mediating tumor resistance to the chemotherapeutic drug gemcitabine. *Science* 2017;**357**:1156−60.
44. Bardou P, Mariette J, Escudié F, Djemiel C, Klopp C. jvenn: an interactive Venn diagram viewer. *BMC Bioinf* 2014;**15**:293.
45. Sinha Ray A, Haikal A, Hammoud KA, Yu ASL. Vancomycin and the risk of AKI: a systematic review and meta-analysis. *Clin J Am Soc Nephrol* 2016;**11**:2132−40.
46. Lestner JM, Hill LF, Heath PT, Sharland M. Vancomycin toxicity in neonates: a review of the evidence. *Curr Opin Infect Dis* 2016;**29**: 237−47.
47. Gu S, Cao B, Sun R, Tang Y, Paletta JL, Wu X, et al. A metabolomic and pharmacokinetic study on the mechanism underlying the lipid-lowering effect of orally administered berberine. *Mol Biosyst* 2015;**11**: 463−74.
48. Liu Y, Liu X, Zhang N, Yin M, Dong J, Zeng Q, et al. Berberine diminishes cancer cell PD-L1 expression and facilitates antitumor immunity *via* inhibiting the deubiquitination activity of CSN5. *Acta Pharm Sin B* 2020;**10**:2299−312.
49. Shah D, Challagundla N, Dave V, Patidar A, Saha B, Nivsarkar M, et al. Berberine mediates tumor cell death by skewing tumor-associated immunosuppressive macrophages to inflammatory macrophages. *Phytomedicine* 2021;**99**:153904.
50. Wculek SK, Cueto FJ, Mujal AM, Melero I, Krummel MF, Sancho D. Dendritic cells in cancer immunology and immunotherapy. *Nat Rev Immunol* 2020;**20**:7−24.
51. Cassetta L, Pollard JW. A timeline of tumour-associated macrophage biology. *Nat Rev Cancer* 2023;**23**:238−57.
52. Galeano Nino JL, Wu H, LaCourse KD, Kempchinsky AG, Baryiames A, Barber B, et al. Effect of the intratumoral microbiota on spatial and cellular heterogeneity in cancer. *Nature* 2022;**611**:810−7.
53. Labeur MS, Roters B, Pers B, Mehling A, Luger TA, Schwarz T, et al. Generation of tumor immunity by bone marrow-derived dendritic cells correlates with dendritic cell maturation stage. *J Immunol* 1999;**162**: 168−75.
54. Li A, Yi M, Qin S, Song Y, Chu Q, Wu K. Activating cGAS−STING pathway for the optimal effect of cancer immunotherapy. *J Hematol Oncol* 2019;**12**:35.
55. Kostic AD, Chun E, Robertson L, Glickman JN, Gallini CA, Michaud M, et al. Fusobacterium nucleatum potentiates intestinal tumorigenesis and modulates the tumor-immune microenvironment. *Cell Host Microbe* 2013;**14**:207−15.
56. Brennan CA, Garrett WS. Fusobacterium nucleatum—symbiont, opportunist and oncobacterium. *Nat Rev Microbiol* 2019;**17**:156−66.
57. Alon-Maimon T, Mandelboim O, Bachrach G. Fusobacterium nucleatum and cancer. *Periodontol* 2000 2022;**89**:166−80.
58. Niccolai E, Baldi S, Nannini G, Gensini F, Papi L, Vezzosi V, et al. Breast cancer: the first comparative evaluation of oncobiome composition between males and females. *Biol Sex Differ* 2023;**14**:37.
59. Wei A, Zhao H, Cong X, Wang L, Chen Y, Gou J, et al. Oral mycobiota and pancreatic ductal adenocarcinoma. *BMC Cancer* 2022;**22**: 1251.
60. Badgeley A, Anwar H, Modi K, Murphy P, Lakshmikuttyamma A. Effect of probiotics and gut microbiota on anti-cancer drugs: mechanistic perspectives. *Biochim Biophys Acta Rev Cancer* 2021;**1875**: 188494.
61. Zhan Y, Zhang Y, Mao C, Li J, Zhao Y, Chen Y, et al. Improved tumor infiltration and immunomodulation for tumor therapy: a pathway based on tetrahedral framework nucleic acids coupled bacterial nanocells. *Nano Lett* 2023;**23**:353−62.
62. Ma S, Sun B, Duan S, Han J, Barr T, Zhang J, et al. YTHDF2 orchestrates tumor-associated macrophage reprogramming and controls antitumor immunity through $CD8^+$ T cells. *Nat Immunol* 2023;**24**: 255−66.
63. Wang L, Jia Q, Chu Q, Zhu B. Targeting tumor microenvironment for non-small cell lung cancer immunotherapy. *Chin Med J Pulm Crit Care Med* 2023;**1**:18−29.
64. Yang L, Li A, Wang Y, Zhang Y. Intratumoral microbiota: roles in cancer initiation, development and therapeutic efficacy. *Signal Transduct Targeted Ther* 2023;**8**:35.
65. Bernardo G, Le Noci V, Ottaviano E, De Cecco L, Camisaschi C, Guglielmetti S, et al. Reduction of *Staphylococcus epidermidis* in the mammary tumor microbiota induces antitumor immunity and decreases breast cancer aggressiveness. *Cancer Lett* 2023;**555**: 216041.

66. Parhi L, Alon-Maimon T, Sol A, Nejman D, Shhadeh A, Fainsod-Levi T, et al. Breast cancer colonization by *Fusobacterium nucleatum* accelerates tumor growth and metastatic progression. *Nat Commun* 2020;**11**:3259.
67. De Filippo C, Cavalieri D, Di Paola M, Ramazzotti M, Poullet JB, Massart S, et al. Impact of diet in shaping gut microbiota revealed by a comparative study in children from Europe and rural Africa. *Proc Natl Acad Sci U S A* 2010;**107**:14691−6.
68. Han ZY, Fu ZJ, Wang YZ, Zhang C, Chen QW, An JX, et al. Probiotics functionalized with a gallium-polyphenol network modulate the intratumor microbiota and promote anti-tumor immune responses in pancreatic cancer. *Nat Commun* 2024;**15**:7096.
69. Wang M, Rousseau B, Qiu K, Huang G, Zhang Y, Su H, et al. Killing tumor-associated bacteria with a liposomal antibiotic generates neoantigens that induce anti-tumor immune responses. *Nat Biotechnol* 2024;**42**:1263−74.
70. Zhou W, Chow K-H, Fleming E, Oh J. Selective colonization ability of human fecal microbes in different mouse gut environments. *ISME J* 2019;**13**:805−23.
71. Wrzosek L, Ciocan D, Borentain P, Spatz M, Puchois V, Hugot C, et al. Transplantation of human microbiota into conventional mice durably reshapes the gut microbiota. *Sci Rep* 2018;**8**:6854.
72. Krych L, Hansen CHF, Hansen AK, van den Berg FWJ, Nielsen DS. Quantitatively different, yet qualitatively alike: a meta-analysis of the mouse core gut microbiome with a view towards the human gut microbiome. *PLoS One* 2013;**8**:e62578.